

Harmonic states in quantum cascade lasers: Frequency-domain analysis and mode-spacing control

Mithun Roy

A Thesis
in
the Department
of
Electrical and Computer Engineering

Presented in Partial Fulfillment of the Requirement
for the Degree of Master of Applied Science (Electrical & Computer Engineering) at
Concordia University
Montréal, Québec, Canada

August 2021

© Mithun Roy, 2021

CONCORDIA UNIVERSITY
SCHOOL OF GRADUATE STUDIES

This is to certify that the thesis prepared

By: Mithun Roy

Entitled: Harmonic states in quantum cascade lasers: Frequency-domain analysis and mode-spacing control

and submitted in partial fulfillment of the requirements for the degree of

Master of Applied Science (Electrical & Computer Engineering)

complies with the regulations of this university and meets the accepted standards with respect to originality and quality.

Signed by the final examining committee:

_____ Chair and Internal Examiner
Dr. Mojtaba Kahrizi

_____ External Examiner
Dr. Muthukumaran Packirisamy

_____ Supervisor
Dr. M. Z. Kabir

Approved by: _____

Dr. Yousef R. Shayan, Chair
Department of Electrical and Computer Engineering

Abstract

Harmonic states in quantum cascade lasers: Frequency-domain analysis and mode-spacing control

Mithun Roy

Quantum cascade lasers (QCLs) are unipolar lasers where lasing transition and carrier transport occur between subbands that result from multiple nanometer-thick quantum wells and barriers formed by the conduction band edges of a semiconductor heterostructure. Since their inception in 1994, QCLs have undergone tremendous improvements with respect to output power, frequency range covered, and maximum operating temperature. As a result, they have become a prominent source of light emitting in the mid- and far-infrared regions of the electromagnetic spectrum.

Multimode behavior of QCLs was a focus of many past works. In a recent comprehensive study, it was found that, if the pumping is increased gradually from threshold, QCLs enter into a harmonic state regime, which is characterized by the lasing of side modes that are separated from each other by multiples of free spectral range (FSR). With a further increase in the pumping, finally, transition into the familiar single-FSR-spaced regime (dense state regime) occurs. Unlike the dense state regime, the harmonic state regime of QCLs has not gone through intense scrutiny, as it is a relatively recent discovery.

In this thesis, a theoretical investigation into the harmonic state regime of QCLs is performed. The work is based on Maxwell's equation and the density matrix (DM) formalism. The two-level DM equations, although commonly employed, ignore many important details of complex carrier transport through a QCL structure. Therefore, here, a three-level DM formalism is employed, which takes into account phenomena such as resonant tunneling and carrier scattering between the three states.

The thesis is mainly divided into two parts. In the first part, starting from the DM-Maxwell equations, an analytical expression for the instability gain of the side modes is derived. This expression can explain the appearance of harmonic states in QCLs. Using this analytical expression, the effects of group velocity dispersion on the harmonic states are studied. In the second part, multimode behavior of QCLs is analyzed using a more general model than that used in the first part. In particular, openness (non-unity facet reflectivity) of the cavity is considered, which was not taken into account in previous works that used the modal expansion method to study QCLs. Using the theory, it is shown that the coating of a facet can be used to excite harmonic states with different mode spacing. Such a control over the generation of harmonic states could make QCLs invaluable for applications such as microwave and terahertz generation, picosecond pulse generation in the mid-infrared frequency range, and broadband spectroscopy.

Acknowledgement

First, I would like to thank my thesis supervisor Prof. Kabir for providing guidance and inspiration throughout the process. He was always ready to share his knowledge and experience with me, which was invaluable for my work. I am also grateful to him for financial support, which enabled me to concentrate fully on my research.

I would like to acknowledge my groupmate Salman for helping me with his computer as well as for engaging in productive discussions. As well, I like to thank my other groupmates, labmates, and friends, especially Farinaz, Iqbal, Suman, Sanjay, Rizvi, Abdullah, Ronak, Milad, Afaz, Ehsan, and Dilshad, without whom my life would have been boring.

Finally, I am grateful to my parents, sister, and uncles for their unconditional love, continuous mental support, and motivation, which gave me the strength to navigate difficult and challenging times.

Table of contents

Table of figures	viii
List of tables	x
List of abbreviations	xi
<hr/>	
Chapter 1: Introduction	1
1.1 Fundamentals of a laser	1
1.2 Quantum cascade lasers	3
1.3 Multimode behavior of QCLs	5
1.4 Problem identification and research objectives	6
1.5 Summary	7
Chapter 2: Theoretical model	8
2.1 Introduction	8
2.2 Maxwell's wave equation	8
2.3 Density matrix formalism	9
2.4 Summary	13
Chapter 3: Harmonic instability in a quantum cascade laser with Fabry-Perot cavity	14
3.1 Abstract	14
3.2 Introduction	14
3.3 Theory	17
3.4 Results and discussion	29
3.5 Summary	43
Chapter 4: Exciting harmonic states in a quantum cascade laser via facet engineering	45
4.1 Abstract	45
4.2 Introduction	45
4.3 Theory: From density matrix and Maxwell's equations to mode equations	47
4.4 Results and discussion	56
4.5 Summary	67
Chapter 5: Conclusion, contribution, and future works	69

5.1	Conclusion	69
5.2	Contribution	70
5.3	Future works	71
<hr/>		
	Appendix A: Three-level system versus two-level system	72
	References	74

Table of figures

Figure 1.1: Schematic diagram of (a) a ring cavity and (b) a Fabry-Perot cavity	2
Figure 1.2: Schematic illustration of the operating principle of a double heterostructure laser	3
Figure 1.3: Simplified diagram showing carrier transport through a typical QCL. RT: Resonant tunneling, LT: Lasing transition, FNS: Fast nonradiative scattering, MQWs: Multiple quantum wells.	4
Figure 2.1: Conduction band diagram and relevant wavefunctions (moduli squared) for the QCL designed in Ref. [19]. The applied bias is 76 kV/cm (lasing threshold). The horizontal axis is in nanometer and the vertical axis is in meV. $\text{In}_{0.53}\text{Ga}_{0.47}\text{As}$ and $\text{Al}_{0.48}\text{In}_{0.52}\text{As}$ are used for the quantum-well and barrier layers, respectively. The thicknesses of the layers for one period, starting from the injection barrier, are as follows (in nm): 5/0.9/1.5/4.7/2.2/4.0/3.0/2.3/2.3/2.2/2.2/2.0/2.0/ <u>2.0/2.3/1.9/2.8/1.9</u> . The underlined layers are n-type doped with Si, resulting in a free electron concentration of $2 \times 10^{17} \text{ cm}^{-3}$. Reproduced from [J. Faist, F. Capasso, C. Sirtori, D. L. Sivco, J. N. Baillargeon, A. L. Hutchinson, S.-N. G. Chu, and A. Y. Cho, “High power mid-infrared ($\lambda \sim 5 \mu\text{m}$) quantum cascade lasers operating above room temperature,” <i>Appl. Phys. Lett.</i> 68 , 3680–3682 (1996)], with the permission of AIP Publishing	10
Figure 2.2: Schematic depiction of carrier transport through the QCL periods under an appropriate bias	12
Figure 3.1: Schematic illustration of carrier transport through the QCL periods under an appropriate bias. Each period is assumed to have three energy levels	20
Figure 3.2: Detuning of the central-mode frequency from the line-center frequency (a) as a function of dephasing time and (b) as a function of GVD. In (a), GVD is taken to be zero, and in (b), the dephasing time is taken to be 0.05 ps. Other parameters are taken from Table 3.1	33
Figure 3.3: (a) Real parts and (b) imaginary parts of the normalized net intensity gains, relative phases of the side modes, and (c) side-mode amplitude ratios for a QCL with $\tau_{\parallel,23} = 0.12 \text{ ps}$ and zero GVD. The QCL is pumped to its instability threshold, i.e., $p \approx 1.23$	36
Figure 3.4: (a) Pumping level triggering the instability, (b) side-mode detuning, (c) logarithm of the amplitude ratio of the side modes, (d) relative phase ϕ , and (e) frequency difference between the cold- and hot-cavity modes (both corresponding to $N_{\text{side,inst}}$) as a function of positive GVD. All the quantities are taken at the instability onset. Dephasing time $\tau_{\parallel,23}$ is taken to be 0.05 ps. Solid triangle and circle are placed at points corresponding to $\alpha = 60000$ and $118000 \text{ fs}^2/\text{mm}$, respectively. The plots of $\text{Re}(g_{1,2})$, $\phi_{1,2}$, and $\log_{10} F_-^*/F_{+1,2} $ versus $\delta\omega$ for these two values of dispersion are shown in Fig. 3.5	38
Figure 3.5: (a) and (d) Frequency dependence of real parts of $g_{1,2}$, (b) and (e) relative	42

<p>phases $\varphi_{1,2}$, and (c) and (f) amplitude ratios $\log_{10} \left \frac{F_-^*}{F_+} \right _{1,2}$ for $\alpha = 60000$ and $118000 \text{ fs}^2/\text{mm}$. The QCL has a dephasing time of 0.05 ps. For $\alpha = 60000 \text{ fs}^2/\text{mm}$ ($118000 \text{ fs}^2/\text{mm}$), the laser is pumped to a value denoted by the solid triangle (circle) in Fig. 3.4(a). Markers in this figure represent the onset-of-instability values. The detuning, the amplitude ratio, and the relative phase at these marked points are also indicated in Figs. 3.4(b)–3.4(d) with the respective markers</p>	
<p>Figure 3.6: (a) side-mode detuning, (b) logarithm of the amplitude ratio of the side modes, (c) relative phase φ, and (d) frequency difference between the cold- and hot-cavity modes (both corresponding to $N_{\text{side,inst}}$) at the instability onset as a function of negative dispersion for a QCL with $\tau_{ ,23} = 0.05 \text{ ps}$</p>	43
<p>Figure 4.1: Schematic illustration of (a) the QCL cavity and (b) carrier transport through the QCL periods</p>	48
<p>Figure 4.2: Scaled threshold function for the uncoated and coated facet. In both cases, the cavity is assumed to be placed in free space</p>	58
<p>Figure 4.3: Ratio of the CF-state coefficients corresponding to the primary mode for $n_3 = 1$ and 2.7. The coating length is set to zero</p>	59
<p>Figure 4.4: (a) Real part of the eigenvalue γ at the onset of instability for three different facet settings. (b) Pumping level triggering single-mode instability for $n_3 = 1, 1.5, 2,$ and 2.7. (c) The relative phase Θ and the side-mode amplitude ratio at the onset of instability for the same four values of n_3. The coating length is zero for (b) and (c)</p>	62
<p>Figure 4.5: Real part of the eigenvalue γ and its breakdown into the linear and nonlinear parts for the same three facet settings considered in Fig. 4.4(a). Pumping level is set to respective p_i</p>	64
<p>Figure 4.6: (a) Scaled threshold function and (b) real part of γ at the onset of instability for four different coating lengths. The refractive index of the coating is $n_2 = 1.55 + 0.00099i$, and the surrounding environment is assumed to be free space. For coating lengths of 0.14 and 0.17 mm, instability occurs at a wavevector detuning of ~ 1 FSR, whereas for 0.3 and 0.45 mm, instability occurs at ~ 21 and ~ 14 FSRs, respectively</p>	65
<p>Figure 4.7: Intensities of the primary and side modes for the same four facet settings considered in Fig. 4.6. The pumping levels at which the mode intensities are found are also shown in this figure. The relative phase Θ is approximately -180° in each of the cases</p>	66
<p>Figure 4.8: (a), (c) Scaled threshold function for two different facet settings, and (b), (d) the corresponding mode intensities. The pumping levels used for the simulation and the corresponding relative phases are also shown in the figure</p>	67

List of tables

Table 3.1: Parameters of the mid-IR QCL used for simulations in this chapter [20,38]	30
Table 4.1: Parameters of the mid-IR QCL used for simulations in this chapter [20,38]	56

List of abbreviations

Amplitude-modulated	AM
Constant-Flux	CF
Density matrix	DM
Equation of motion	EoM
Fabry-Perot	FP
Fourier transform	FT
Four-wave mixing	FWM
Free spectral range	FSR
Frequency-modulated	FM
Full-width-half-maximum	FWHM
Gauge fixing requirement	GFR
Group velocity dispersion	GVD
Lower lasing state	LLS
Mid-infrared	Mid-IR
Partial differential equation	PDE
Population pulsation	PP
Quantum cascade laser	QCL
Resonant tunneling	RT
Rotating-wave approximation	RWA
Slowly varying	SV
Spatial hole burning	SHB
Steady-state <i>ab initio</i> laser theory	SALT
Terahertz	THz
Upper lasing state	ULS

Chapter 1: Introduction

1.1 Fundamentals of a laser

Lasers are one of the most important discoveries of the twentieth century. Modern life cannot be imagined without lasers. They have numerous applications in various fields, such as spectroscopy, medical imaging, microwave and terahertz photonics, and astronomy.

Broadly speaking, a laser is a device that amplifies light, just like transistors that amplify electrical signals at different frequencies. Lasers generate coherent and collimated electromagnetic waves of frequencies starting from the ultraviolet region up to the far-infrared region of the electromagnetic spectrum [1]. They can be of different sizes and can deliver a wide range of power depending on the applications, ranging from the laser pointers used in classrooms to powerful gas lasers used in industry.

The operating principle of a laser is based on a phenomenon called stimulated emission. Consider a material system having just two discrete energy levels. When an electromagnetic field of frequency close to the frequency corresponding to the energy difference between the two levels is incident on the material, the electrons face a sinusoidal potential perturbation. The probability of the electrons in the lower energy level performing an upward jump is the same as the probability of the electrons in the upper energy level performing a downward jump [2]. Photon emission due to this downward jump under the influence of an electromagnetic field is called stimulated emission. Now, if the number of electrons (population) at the lower level is higher than that in the upper level, which is the case if the material is in thermal equilibrium, then a net absorption of the incident photons will occur. However, if the population in the upper state is higher, a net downward transition of electrons will occur, emitting photons at the same frequency and polarization as those of the incident photons. As a result, the emitted light will be more intense than the incident light and will be coherent.

Therefore, population inversion is an essential ingredient for a laser to work. In order to create population inversion, one needs to supply energy from outside (pumping), thus driving the material out of thermal equilibrium. Pumping can be of any form, e.g., supplying electrical current

into the medium, or optically loading carriers in the upper state. The other ingredient necessary for a laser is an optical resonator (cavity), in which the medium (gain medium or active medium) is placed. Light in the cavity bounces back and forth upon repeated reflection at the end mirrors, gaining intensity each time while passing through the gain medium. At some point, after the transients have died out, the intensity becomes constant. This situation is referred to as the gain saturation being reached. Typically, two types of cavities are employed, a Fabry-Perot or a ring cavity. Both types of cavities are depicted in Fig. 1.1.

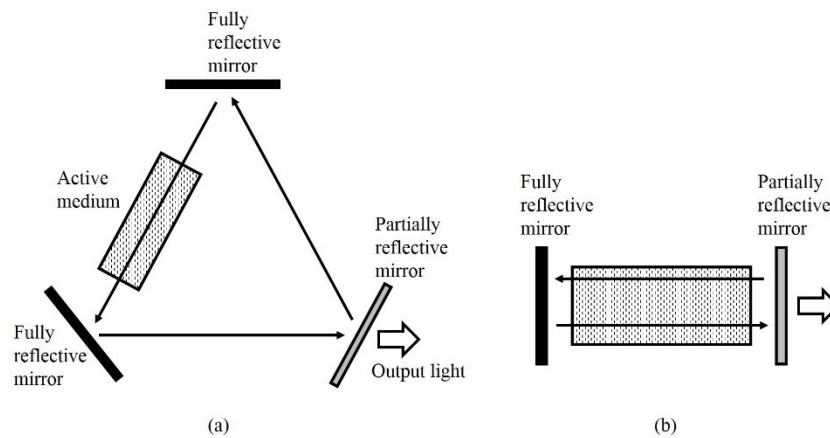


Figure 1.1: Schematic diagram of (a) a ring cavity and (b) a Fabry-Perot cavity.

Lasers can be roughly put into the following categories based on the material of the gain medium [3].

Solid state lasers: Gain medium is solid, often in the form of a crystal or a rod. Typically, it is doped with metallic ions. Pumping is done via optical means. Some common examples include ruby laser, Ti:Sapphire laser etc.

Gas lasers: Active region is in gaseous form. Common gas lasers include CO₂ laser, helium-neon laser etc. In CO₂ laser, lasing occurs due to transition of CO₂ molecules into lower vibration levels.

Semiconductor lasers: As the name suggests, semiconductors, commonly III-V materials, are employed as the gain medium. Pumping is done electrically, i.e., electrical current is injected in order to achieve population inversion. Under electrical bias, electrons undergo lasing transition from a conduction band to a valence band, thus recombining with a hole in the valence band. A common example is a diode laser. As well, Electrons can perform radiative transition within subbands belonging to a conduction band, such as in quantum cascade lasers.

Dye lasers: A liquid solution of organic materials is employed as the active medium. Under optical illumination (pumping), lasing occurs due to fluorescence.

1.2 Quantum cascade lasers

In conventional semiconductor lasers, population inversion is achieved between a conduction band and a valence band. Figure 1.2 depicts the operating principle of a double heterostructure semiconductor laser in terms of a simplified energy band diagram. Under the influence of an external bias (forward bias), electrons from the n-type layer and holes from the p-type layer are injected into the sandwiched active layer, thus resulting in population inversion. Lasing occurs as a result of the electrons falling from the conduction band and recombining with the holes in the valence band. Although this type of interband lasers is cheap and easy to fabricate, there is a problem: the frequency of the lasing light is determined by the bandgap of the material, which cannot be easily changed. In particular, the conventional semiconductor lasers poorly cover the mid- to far-infrared region of the electromagnetic spectrum [4].

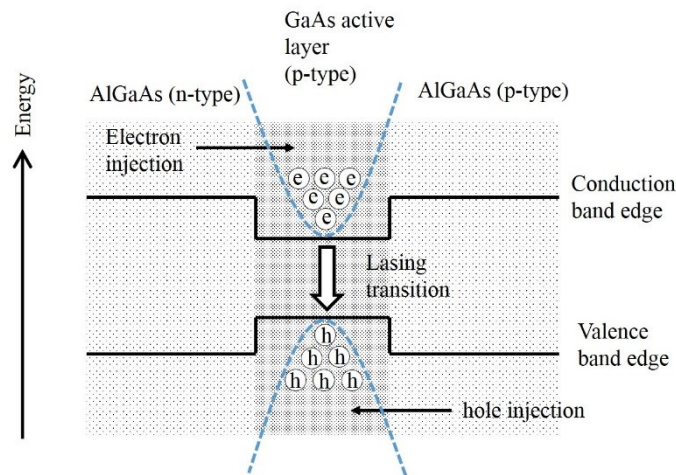


Figure 1.2: Schematic illustration of the operating principle of a double heterostructure laser.

Quantum cascade lasers (QCLs) are unipolar lasers where lasing transition occurs between subbands that belong to a conduction band, as opposed to interband lasers where conduction to valence band transition is involved. Figure 1.3 shows the basic operating principle of a QCL. Layers of semiconducting materials, typically III-V materials, are grown in a way so that the corresponding conduction band edges form many repetitions of a quantum barrier-well-barrier

structure. These quantum wells and barriers result in bound states, also known as subbands, through which electron transport occurs. The widths of the materials (thickness of the quantum wells and barriers) are carefully chosen so that electrons are injected efficiently into the upper lasing state under appropriate DC biases. Although there exist other electron injection mechanisms, resonant tunneling mechanism is commonly employed, where the ground state of a preceding quantum well is designed to be located very close in energy to the upper lasing state of the following quantum well. Electrons then efficiently tunnel from the ground state into the upper lasing state. In addition, the lower lasing state is designed to have a very short carrier lifetime. As a result, population inversion occurs, and lasing ensues. Moreover, carrier transport in a QCL is periodic in nature, i.e., the same sequence of transport events is repeated as electrons traverse the structure (Fig. 1.3). Thus, one electron produces multiple photons—one photon per period.

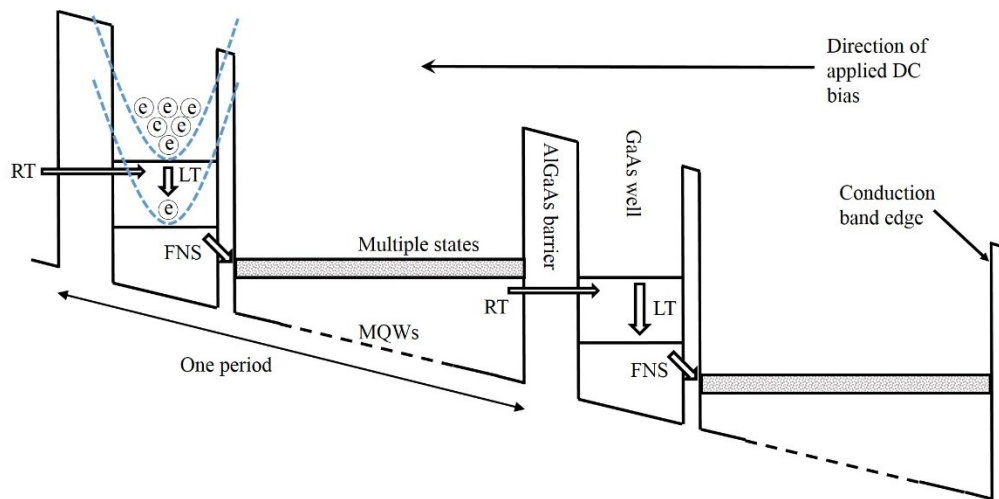


Figure 1.3: Simplified diagram showing carrier transport through a typical QCL. RT: Resonant tunneling, LT: Lasing transition, FNS: Fast nonradiative scattering, MQWs: Multiple quantum wells.

In QCLs, lasing frequency is determined by the energy difference between lasing subbands. Just by changing the thickness of the materials, one can vary emission frequency. Thus, the discovery of these lasers gave us freedom from “bandgap slavery.” Particularly, the emission range of QCLs covers both the mid-infrared and terahertz region of the electromagnetic spectrum. Moreover, the periodic nature of the carrier transport (hence the name cascade) results in a high differential quantum efficiency, i.e., high output power from the laser can be obtained.

The idea of light amplification by intersubband transitions was first proposed by Kazarinov and Suris in 1971 [5]. However, due to technological issues, it was not until 1994 when the first intersubband laser (QCL) was demonstrated by Faist and coworkers [6]. The device operated in the mid-infrared region, providing limited optical power at cryogenic temperatures (maximum operating temperature was ~ 90 K). Then, in 2002, continuous-wave operation of QCLs at room temperature was achieved [7]. In the same year, another milestone was reached when the operating frequency of QCLs was extended into the terahertz range [8]. Since the energy difference between the lasing states in terahertz QCLs is small, they operated at cryogenic temperatures for years. Very recently, researchers have been able to raise the operating temperature above that of a thermoelectric cooler (235 K), demonstrating a maximum operating temperature of 250 K [9]. Besides, improvements were achieved in terms of high-power delivery and high wall-plug efficiency [10,11].

1.3 Multimode behavior of QCLs

Consider a Fabry-Perot cavity of length L with unity facet reflectivity. The cavity is assumed to be filled with a medium of refractive index n . The cavity does not just support any wavevectors; it supports a wavevector for which the corresponding spatial variation can replicate itself after each round trip. These allowed wavevectors are referred to as the longitudinal modes of the cavity. The angular frequencies of the longitudinal modes are given by $\omega_i = i\pi c/(Ln)$, where i is an integer and c is the speed of light in free space. The frequency spacing between the two consecutive modes, $\pi c/(Ln)$, is called the free spectral range (FSR) of the laser. If the refractive index is independent of frequency, i.e., if there is no group velocity dispersion (GVD), the modes will be equally spaced in frequency. However, in reality, no material is free of GVD. As a result, the modes always walk off to some degree from being equally spaced.

The gain spectrum of a QCL is not flat; rather it typically takes the shape of a Lorentzian, where the gain peaks at some frequency and gradually falls off as the frequency detuning from the gain-peak frequency increases. At a pumping slightly higher than lasing threshold, the longitudinal mode whose frequency is close to the gain-peak frequency lases, and the QCL operates in a single mode regime. As the pumping is increased slowly, the QCL enters into a harmonic state regime,

which is characterized by the appearance of side modes that are located multiples of FSRs away from each other. Although GVD causes the cavity modes to be spaced in a nonuniform way, the side modes in a harmonic state regime were shown to be equally spaced [12]. This uniform spacing occurs due to the optical nonlinearity of the gain medium. When a laser emits multiple modes that are equally spaced in frequency, the emission spectrum is referred to as a *frequency comb*. Finally, if the pumping is increased further, the operating regime changes into a more familiar single-FSR-spaced (dense state) regime. Although harmonic state regime is a general phenomenon for QCLs, it was definitively discovered only recently, in 2016 [13], because the harmonic state is very sensitive to certain experimental conditions. Even placing a poorly aligned collimating lens between a QCL and a spectrometer or a rapid increase in the pumping current can cause the laser to undergo transition from the harmonic state regime to the dense state regime. Harmonic frequency comb has applications in microwave and terahertz generation, picosecond pulse generation in the mid-infrared frequency range, and broadband spectroscopy [14].

If the pumping is not too high, QCLs emit frequency combs while operating in the dense state regime as well. The operation of a QCL as a dense frequency comb was first achieved in the mid-infrared frequency region [15]. The device had a low GVD and operated in a free-running mode. Later, dense frequency comb was achieved using a terahertz QCL as well [16]. The device also operated in a free-running mode, and a special dispersion compensation technique was employed, in that a chirped corrugation was etched into the facet of the QCL. These devices did not produce pulses in time domain. Rather, they produced output of almost constant intensity. In another words, the devices emitted frequency-modulated combs. Very recently, frequency comb operation of free-running ring QCLs has been demonstrated as well [17].

1.4 Problem identification and research objectives

The harmonic state regime of QCLs was studied in Refs. [12,13] by using a carrier transport model that considers only two states, i.e., lasing states. However, in a real QCL, transport involves a set of complex events, such as resonant tunneling and carrier scattering between many energy states. Moreover, in those works, the facets of the cavity were assumed to be perfectly reflective, i.e., closed-cavity assumption was employed. Furthermore, a detailed investigation into the effects of GVD on the harmonic states was not performed. However, in order to better understand the

regime as well as to be able to engineer the spacing between the modes, consideration of these factors in the analysis is necessary.

Therefore, the research objectives are as follows:

- a. Construct an analytical frequency-domain theory for multimode behavior of Fabry-Perot QCLs by considering carrier transport involving three states, GVD, and cavity openness (nonunity facet reflectivity).
- b. Control the frequency spacing between the modes in a harmonic state by varying the attributes of a facet coating.

1.5 Summary

In this chapter, an introductory discussion on lasers has been presented. Also, in simple terms, the operating principle of a QCL and its multimode behavior have been discussed. In addition, the research objective has been detailed. The remainder of this thesis is organized as follows: The second chapter discusses the theoretical background necessary to analyze multimode behavior of QCLs. The third chapter focuses on the study of the harmonic state regime of QCLs by using a model that considers resonant tunneling and GVD. The closed-cavity assumption is employed for analysis in this chapter. In the fourth chapter, a multimode theory that takes into account openness of the cavity is presented. Using the theory, a way to control the spacing between the modes in a harmonic state is shown. Finally, the thesis concludes with a summary, contribution, and future works in chapter five.

Chapter 2: Theoretical model

2.1 Introduction

In quantum cascade lasers (QCLs), conduction band edges form multiple quantum wells and barriers which give rise to localized energy states. To describe carrier transport through these states, the density matrix (DM) formalism is typically adopted. Moreover, Maxwell's wave equation is used to describe the propagation of the laser field through a QCL. Since the carrier transport and the laser field are inherently coupled, one needs to solve the DM and Maxwell's equations simultaneously in order to analyze multimode behavior of a QCL. This chapter discusses the wave equation and the DM formalism, which will be used in the next two chapters.

2.2 Maxwell's wave equation

To derive the wave equation, one would start by writing Faraday's and Ampere's laws as follows, which describe the time evolutions of the electric field \vec{E} inside a QCL and the corresponding magnetic field strength vector \vec{H} :

$$\nabla \times \vec{E} = -\frac{\partial \vec{B}}{\partial t}, \quad (2.1)$$

$$\nabla \times \vec{H} = \frac{\partial \vec{D}_e}{\partial t}. \quad (2.2)$$

Here, \vec{B} represents the magnetic flux density and \vec{D}_e is the electric displacement vector. QCLs are made of nonmagnetic materials, so one can write $\vec{B} = \mu_0 \vec{H}$, where μ_0 is the magnetic permeability of free space. Also, the displacement vector can be expressed as $\vec{D}_e = \epsilon_0 \vec{E} + \vec{P}$, where ϵ_0 is the free-space permittivity and \vec{P} denotes the total electric polarization. Now, consider that the heterostructure of the QCL is grown in the z -direction. Then, according to the selection rules for intersubband transitions, only the resonator modes that have an electric field component along the z -direction will be amplified [18]. Therefore, supposing that the QCL has a slab waveguide structure, the focus can be limited only to the transverse electromagnetic modes [3]. Thus, Eqs. (2.1) and (2.2) reduce to [3]

$$\frac{\partial}{\partial t} E_z(x,t) = \frac{1}{\varepsilon_0 \varepsilon_r} \left[\frac{\partial}{\partial x} H_y(x,t) - \frac{\partial}{\partial t} P_z(x,t) \right], \quad (2.3)$$

$$\frac{\partial}{\partial t} H_y(x,t) = \frac{1}{\mu_0} \frac{\partial}{\partial x} E_z(x,t). \quad (2.4)$$

Here, the x -axis denotes the propagation direction and $E_z(x,t)$ is the component of \vec{E} in the z -direction averaged over the y - and z -dimensions. Moreover, $H_y(x,t)$ is the component of \vec{H} in the y -direction averaged over the y - and z -dimensions, and $P_z(x,t)$ is defined in a similar way. Finally, by eliminating H_y from Eqs. (2.3) and (2.4), one gets the wave equation

$$\frac{\partial^2}{\partial x^2} E_z - \frac{1}{c^2} \frac{\partial^2}{\partial t^2} E_z = \frac{1}{\varepsilon_0 c^2} \frac{\partial^2}{\partial t^2} P_z, \quad (2.5)$$

where the relation $c^2 = 1/(\varepsilon_0 \mu_0)$ has been used with c being the speed of light in free space. Note that P_z represents the total polarization, i.e., the sum of the linear polarization due to the background host medium and the nonlinear polarization associated with the intersubband transition. Equation (2.5) does not explicitly include any term that represents waveguide loss; however, it can be considered either by adding a phenomenological loss term or by taking the refractive index of the background medium to be complex.

2.3 Density matrix formalism

First, consider electron transport through the multiple quantum wells and barriers in a real QCL. Figure 2.1 shows the conduction band diagram along with the relevant energy levels for the mid-infrared QCL designed in Ref. [19]. The laser is made of an InGaAs/AlInAs heterostructure, where the $\text{In}_{0.53}\text{Ga}_{0.47}\text{As}$ layers represent quantum wells and the $\text{Al}_{0.48}\text{In}_{0.52}\text{As}$ layers represent quantum barriers. Lasing starts at an external bias of 76 kV/cm. The region where lasing transition occurs is the active region, which consists of a thin well and two thick wells. Lasing transition is denoted by a wavy arrow, occurring between states $|3\rangle$ (upper lasing state) and $|2\rangle$ (lower lasing state) with an emission wavelength of $\sim 5 \mu\text{m}$. The energy difference between states $|2\rangle$ and $|1\rangle$ is designed to be close to the longitudinal optical phonon energy of InGaAs (34 meV), which ensures fast $|2\rangle \rightarrow |1\rangle$ electron scattering rate and therefore helps achieve population inversion. From $|1\rangle$, electrons scatter to the injector region, which consists of a manifold of states (injector

states). The spatial extent of these states takes the form of a funnel, hence the name “funnel injector.” Finally, electrons (almost) resonantly tunnel from the injector ground state $|g\rangle$ to the upper lasing state of the next period (through the injection barrier), and the above cycle of carrier transport continues. Note that the described design is just one of the many designs that exist in the literature [20].

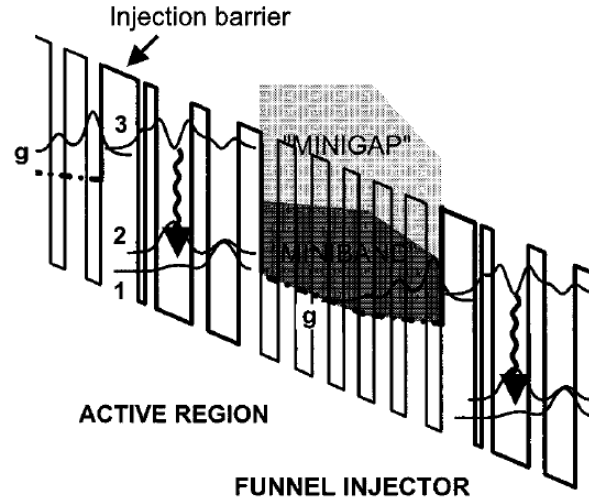


Figure 2.1: Conduction band diagram and relevant wavefunctions (moduli squared) for the QCL designed in Ref. [19]. The applied bias is 76 kV/cm (lasing threshold). The horizontal axis is in nanometer and the vertical axis is in meV. $\text{In}_{0.53}\text{Ga}_{0.47}\text{As}$ and $\text{Al}_{0.48}\text{In}_{0.52}\text{As}$ are used for the quantum-well and barrier layers, respectively. The thicknesses of the layers for one period, starting from the injection barrier, are as follows (in nm): $5/0.9/1.5/4.7/2.2/4.0/3.0/2.3/2.3/2.2/2.2/2.0/2.0/2.0/2.3/1.9/2.8/1.9$. The underlined layers are n-type doped with Si, resulting in a free electron concentration of $2 \times 10^{17} \text{ cm}^{-3}$. Reproduced from [J. Faist, F. Capasso, C. Sirtori, D. L. Sivco, J. N. Baillargeon, A. L. Hutchinson, S.-N. G. Chu, and A. Y. Cho, “High power mid-infrared ($\lambda \sim 5 \mu\text{m}$) quantum cascade lasers operating above room temperature,” *Appl. Phys. Lett.* **68**, 3680–3682 (1996)], with the permission of AIP Publishing.

While modeling carrier transport through a QCL, one does not take into account all the states that the electrons travel through, since it would make the computation prohibitively intensive. Most commonly, only upper and lower lasing states are considered, and carrier transport is described by the two-level DM equations, also known as Bloch equations. Bloch equations have the following form [21]:

$$\dot{\rho}_{33} - \dot{\rho}_{22} = \frac{w_{\text{eq}} - (\rho_{33} - \rho_{22})}{\tau_{32}} + i2aE_z(\rho_{32} - \rho_{32}^*) + D \frac{\partial^2 (\rho_{33} - \rho_{22})}{\partial x^2}, \quad (2.6)$$

$$\dot{\rho}_{32} = -(\mathbf{i}\omega_{23} + \tau_{\parallel}^{-1})\rho_{32} + iaE_z(\rho_{33} - \rho_{22}), \quad (2.7)$$

where ρ_{33} and ρ_{22} represent the normalized populations in the upper and lower lasing states, respectively, ρ_{32} denotes the coherence between the lasing states, and the overdots denote time derivatives of the corresponding quantities. Moreover, w_{eq} represents the population inversion that would exist in the absence of lasing, τ_{32} is the carrier lifetime corresponding to $|3\rangle \rightarrow |2\rangle$ scattering rate, $a = ez_{23}/\hbar$, ez_{23} represents the corresponding dipole matrix element, D is the diffusion coefficient, ω_{23} is the optical transition frequency (corresponding energy difference/ \hbar), and τ_{\parallel}^{-1} denotes the dephasing rate of electrons between the lasing states. Often, in an attempt to capture the complex nature of carrier transport through a QCL, τ_{32} is replaced by an equivalent time parameter known as the gain recovery time T_1 . For a typical mid-infrared QCL, the gain recovery time is ~ 2 ps [22].

Although commonly used for simplicity, the above two-level model leaves out many important details of the carrier transport, such as resonant tunneling and carrier scattering into the other energy states. Figure 2.2 shows the schematic diagram of a more realistic model of carrier transport through a typical QCL. In particular, in addition to the lasing states $|3\rangle$ and $|2\rangle$, a third energy state $|1g\rangle$ (or $|1g'\rangle$ depending upon the period) has been added. This state takes into consideration the combined effect of $|1\rangle$ and the injector states in Fig 2.1 on the carrier transport (compare Fig. 2.2 with Fig. 2.1). So, for this three-level model, the population equations can be written as

$$\dot{\rho}_{1g,1g} = -\frac{J_{1g,3}}{e} - \frac{J_{1g,2}}{e} + \tau_{3,1g'}^{-1}\rho_{33} + \tau_{2,1g'}^{-1}\rho_{22} + D \frac{\partial^2 \rho_{1g,1g}}{\partial x^2}, \quad (2.8)$$

$$\dot{\rho}_{33} = \frac{J_{1g,3}}{e} - (\tau_{32}^{-1} + \tau_{3,1g'}^{-1})\rho_{33} + iaE_z(\rho_{32} - \rho_{32}^*) + D \frac{\partial^2 \rho_{33}}{\partial x^2}, \quad (2.9)$$

$$\dot{\rho}_{22} = \frac{J_{1g,2}}{e} + \tau_{32}^{-1}\rho_{33} - \tau_{2,1g'}^{-1}\rho_{22} + iaE_z(\rho_{32}^* - \rho_{32}) + D \frac{\partial^2 \rho_{22}}{\partial x^2}, \quad (2.10)$$

where $\rho_{i,i}$ (or ρ_{ii}) denotes the normalized population in state $|i\rangle$ as before, $J_{i,j}$ represents the second-order currents due to resonant tunneling, and $\tau_{i,j}$ (or τ_{ij}) is the carrier lifetime corresponding to $|i\rangle \rightarrow |j\rangle$ scattering rate. The coherence equation, however, remains the same as Eq. (2.7).

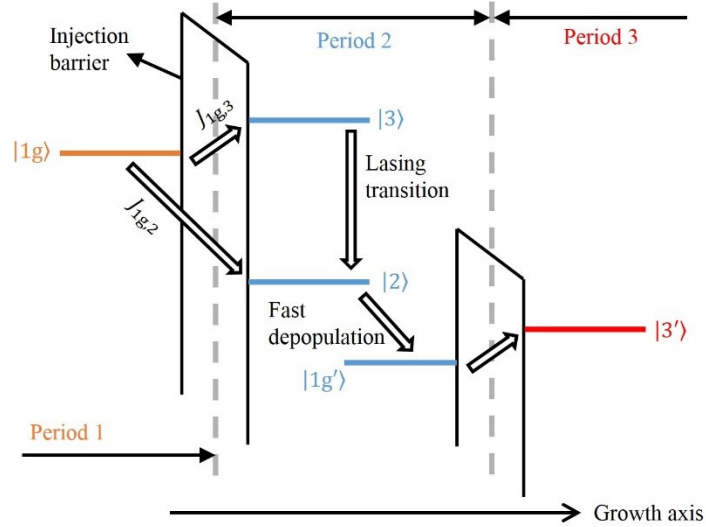


Figure 2.2: Schematic depiction of carrier transport through the QCL periods under an appropriate bias.

Maxwell's equation and the DM equations are coupled via the nonlinear part of the total polarization P_z , i.e., $P_{\text{three-level}}$, which acts as a source term for Eq. (2.5). $P_{\text{three-level}}$ depends on the coherence according to

$$P_{\text{three-level}} = -N\Gamma a\hbar(\rho_{32} + \rho_{32}^*), \quad (2.11)$$

where N denotes the concentration of free electrons in the QCL and Γ represents the overlap factor between the optical field and the active region. Therefore, the population equations (2.8)–(2.10), the coherence equation (2.7), Maxwell's equation (2.5), and the coupling equation (2.11) represent the complete set of equations which will be used in later chapters to describe multimode behavior of QCLs.

2.4 Summary

In this chapter, the derivation of the wave equation from Faraday's and Ampere's laws has been shown. Also, the band diagram of a real QCL has been presented, and in light of this, the two- and three-level DM equations have been discussed.

Chapter 3: Harmonic instability in a quantum cascade laser with Fabry-Perot cavity

The content of this chapter has been taken from my publication in Ref. [23].¹

3.1 Abstract

A new state of instability called harmonic instability, which is characterized by the appearance of side modes separated by multiple of free spectral range from each other, was discovered in quantum cascade lasers (QCLs) a few years ago. However, a detailed analysis using a model beyond the two-level density-matrix (DM) equations as well as incorporating phenomena such as the detuning of the primary-mode frequency from the line-center frequency and the frequency dependence of the background refractive index, resulting in group velocity dispersion (GVD), has not been performed yet. In this chapter, we present a comprehensive analysis of harmonic instability in a QCL with Fabry-Perot (FP) cavity. Starting from the three-level DM equations, which include resonant tunneling phenomenon and scattering rates between all three states, and then by using Maxwell's equation, we derive a closed-form expression for the gain of the side modes, from which quantities pertinent to instability can be determined. We also take the aforementioned phenomena into account in our theory. By using our theory, we show the way of determining the primary-mode detuning from the line center. Furthermore, we study the effects of GVD on instability in detail, showing that the output from an FP QCL demonstrates the characteristic of a frequency-modulated wave up to a certain value of dispersion. Above this value, because of the significant deviation of the side-mode amplitude ratio from unity, the output shows neither frequency-modulated-like nor amplitude-modulated-like behavior.

3.2 Introduction

A laser, when pumped to its threshold, starts oscillating at a single mode, also referred to as primary or central mode. As the pumping is increased slowly, the intensity of the single-mode light increases. When the pumping reaches a specific value known as the instability threshold or

¹ M. Roy and M. Z. Kabir, "Harmonic instability in a quantum cascade laser with Fabry-Perot cavity," *Journal of Applied Physics* **128**, 043105 (2020).

second threshold, the laser becomes unstable and emits multiple modes. For a unidirectional laser, in the single-mode regime, the population inversion remains constant at its threshold value everywhere inside the cavity. As a result, the linear gain, also known as the incoherent gain or Lorentzian gain, of the side modes does not vary with pumping and is smaller than the loss (the total loss is comprised of waveguide and mirror loss). Therefore, the linear gain alone cannot pull the side modes above threshold in a unidirectional laser. In a laser cavity, photons of a frequency different from the frequency of the central mode always exist. They, together with the central-mode photons, create an intensity modulation at the difference frequency of the two fields, which, in turn, causes population inversion to vary at that difference frequency. This is known as population pulsation (PP). Due to PP, side modes at the corresponding frequencies experience a gain referred to as the nonlinear gain (also known as the coherent or parametric gain) that varies with pumping. For a sufficiently high pumping level, the total contribution of incoherent and coherent gains overcomes losses at a pair of frequencies—one on each side of the central mode. Consequently, the corresponding side modes start to lase, and the laser becomes unstable. This instability in a traveling-wave laser is known as the Risken-Nummedal-Graham-Haken instability [24,25].

For a standing-wave laser, provided that the diffusion coefficient is not too high, population inversion does not remain constant everywhere inside the cavity in the single-mode regime. It assumes the form of a grating, a phenomenon known as spatial hole burning (SHB), which also varies with the pumping. SHB is responsible for the lowering of instability threshold in standing-wave lasers [13,26,27].

Single-mode instability in quantum cascade lasers (QCLs) was a focus of many past works [13,26,27,28,29]. In particular, Gordon *et al.* [27] analyzed instability in Fabry-Perot (FP) QCLs by treating the effects of SHB and PP separately. However, Mansuripur *et al.* [13] argued that one should treat the effects of SHB and PP simultaneously while analyzing instability. They indeed were able to explain the origin of a new state of instability in QCLs, namely harmonic instability. It was experimentally shown in Ref. [13] that, when primary mode in an FP QCL becomes unstable, which occurs at a pumping level not far from lasing threshold, it enters into a harmonic-instability regime, characterized by the occurrence of side modes that are located multiple of free

spectral range (FSR) apart from each other. If the pumping is kept increasing, the laser enters into more familiar single-FSR regime, where the output spectrum is comprised of single-FSR-spaced modes. Though harmonic instability is a general phenomenon for QCLs, it had been observed rarely in prior works [30] because the harmonic state is very sensitive to certain experimental conditions. Even placing a poorly aligned collimating lens between a QCL and a spectrometer or a rapid increase in the pumping current can cause the laser to undergo a transition from the harmonic-instability regime to the single-FSR regime [13,14]. Recently, the frequency-comb nature (i.e., the uniform-spacing nature) of the modes in the harmonic-instability regime was demonstrated [12]. Harmonic frequency comb has applications in microwave and terahertz generation, picosecond pulse generation in the mid-infrared (mid-IR) frequency range, and broadband spectroscopy [14].

In the previous work [13], each period of a QCL was considered to have two energy levels, and thus, the two-level density-matrix (DM) equations, also known as Bloch equations, were used in the analysis of harmonic instability. However, in reality, each period of a QCL has more than two states, and resonant tunneling (RT) is often exploited in the laser design as a mechanism to inject carriers from the injector region of the $(s-1)$ -th period into the active region of the s -th period, where s represents the period number. Therefore, in order to describe the complex carrier transport in actual devices and thus accurately predict the instability, we need a model beyond the two-level DM equations. Moreover, the detuning of the primary-mode frequency from line-center frequency (i.e., optical transition frequency) was not taken into consideration. In addition, the frequency-dependent nature of the background refractive index, which causes the group velocity of light inside the cavity to depend on frequency (i.e., group velocity dispersion), was not considered. In Ref. [12], though group velocity dispersion (GVD) was considered, a rigorous theory leading to a closed-form expression for the gain of the side modes was not developed. Also, the effects of GVD on instability were not fully explored. Therefore, a thorough study of harmonic instability in QCLs, in order to make QCLs more appealing for the aforementioned applications, is essential.

In this chapter, we present a detailed analysis of harmonic instability in a QCL having an FP cavity. We model each QCL period to have three energy states and describe carrier transport

by using a DM model that accounts for RT mechanism and scattering rates between all three states. We solve coupled Maxwell-DM equations by assuming the laser spectrum to be comprised of three modes, namely a primary mode and two weak side modes, and thus derive a closed-form expression for the gain of the side modes. The analytical model can determine different quantities pertaining to instability, such as the pumping level that causes the laser to be unstable and the side-mode detuning at the onset of instability. Our theory takes the detuning of the primary mode frequency from line-center frequency and GVD into consideration. The theory works for lasing operation up to the onset of instability.

With the help of our theory, we show how to determine the central-mode detuning. Moreover, we study the effects of GVD on laser instability in detail. Though FP QCLs generally emit frequency-modulated (FM) light [31], this study reveals that FP QCLs show FM-like behavior up to a certain value of dispersion. When the dispersion exceeds this value, the ratio of the amplitudes of the side modes deviates considerably from unity, and therefore, the output shows neither FM-like nor amplitude-modulated-like (AM-like) behavior.

The remainder of this chapter is organized as follows: In Sec. 3.3, we present a theory of harmonic instability in an FP QCL. In Sec. 3.4, by using our theory, we explain the process of determining the central-mode detuning and also study the influence of GVD. Finally, we conclude our work with a summary in Sec. 3.5.

3.3 Theory

We formulate the theory of harmonic instability by following an approach similar to those in Refs. [13] and [32]. Before going into the derivation, we give an outline of our approach. First, we assume that the laser electric field is composed of three spatially orthonormal modes, i.e., a primary mode and two weak side modes, and we represent the elements of the DM in terms of slowly varying (SV) amplitudes and rapidly varying exponential functions. Second, by putting these expansions into the DM equations, we get a system of coupled partial differential equations (PDEs), and then we solve this system, obtaining the steady-state solution of the SV amplitudes. Third, we plug these solutions into Maxwell's equation, and by exploiting orthogonality of the lasing modes, we obtain an equation of motion (EoM), i.e., an equation describing the time

dependence of the mode amplitude, for each of the modes. Fourth, we solve the EoM for the primary mode, thereby finding the steady-state value of the primary-mode amplitude and the corresponding frequency. Finally, we assume that the side-mode amplitudes experience exponential gain (or decay), plug the values of the primary-mode amplitude and frequency into the side-mode EoMs, and find the final equation for the gain of the side modes. This equation provides all the relevant information regarding the instability.

We begin by assuming that an electric field $E_z(x, t)$, directed along the z -axis, propagates along the x -axis through a QCL. The QCL has an active medium consisting of many heterostructure periods, and each period is considered to have three energy levels. Under an appropriate DC bias, the carrier transport through the periods takes place, as shown in Fig. 3.1, according to the following sequence: First, from the ground (injector) state $|1\rangle$ of the $(s-1)$ -th period, electrons predominantly scatter to the upper lasing state $|2\rangle$ of the s -th period by RT; next, they mainly undergo lasing transition, reaching the lower lasing state $|3\rangle$ of the same period; finally, electrons relax to the ground (collector) state $|1'\rangle$ of the s -th period via phonon and other relevant scattering mechanisms. We describe carrier transport by the following simplified DM equations:

$$\dot{\rho}_{11} = -\frac{J_{12}}{e} - \frac{J_{13}}{e} + \tau_{21'}^{-1}\rho_{22} + \tau_{31'}^{-1}\rho_{33} + D\frac{\partial^2\rho_{11}}{\partial x^2}, \quad (3.1)$$

$$\dot{\rho}_{22} = \frac{J_{12}}{e} - (\tau_{23}^{-1} + \tau_{21'}^{-1})\rho_{22} + iaE_z(\rho_{23} - \rho_{23}^*) + D\frac{\partial^2\rho_{22}}{\partial x^2}, \quad (3.2)$$

$$\dot{\rho}_{33} = \frac{J_{13}}{e} + \tau_{23}^{-1}\rho_{22} - \tau_{31'}^{-1}\rho_{33} + iaE_z(\rho_{23}^* - \rho_{23}) + D\frac{\partial^2\rho_{33}}{\partial x^2}, \quad (3.3)$$

$$\dot{\rho}_{23} = -(\mathbf{i}\omega_{23} + \tau_{\parallel,23}^{-1})\rho_{23} + iaE_z(\rho_{22} - \rho_{33}), \quad (3.4)$$

where ρ_{ij} is the corresponding DM element, the overdots represent the time derivatives of the corresponding quantities, τ_{ij}^{-1} and $\tau_{\parallel,ij}^{-1}$ denote the scattering rate and the dephasing rate of electrons between the states $|i\rangle$ and $|j\rangle$, D is the diffusion coefficient, ω_{23} is the optical transition frequency ($\omega_{23} = \varepsilon_{23}/\hbar$ with ε_{23} denoting the energy difference between the states $|2\rangle$ and $|3\rangle$),

$a = ez_{23}/\hbar$, ez_{23} represents the corresponding dipole matrix element, and J denotes the second-order tunneling current density between relevant states. Since single-mode instability in an FP QCL occurs at a pumping level not far above the lasing threshold [13], we assume that the energy differences between the states within a period and hence the carrier scattering rates between them do not change with pumping once lasing threshold is reached. Supposing that the energy of state $|1\rangle$ is lower than or equal to that of $|2\rangle$, we write the tunneling current densities as $J_{12} = e\alpha_{12}(\rho_{11}\beta_{12} - \rho_{22})$ and $J_{13} = e\alpha_{13}(\rho_{11} - \rho_{33}\beta_{13})$, where $\alpha_{ij} = 2(\hbar\Omega_{ij})^2 \gamma_{ij} / [\hbar(\varepsilon_{ij}^2 + \gamma_{ij}^2)]$, $\beta_{ij} = \exp(-|\varepsilon_{ij}|/k_B T_e)$ [33,34]; $\hbar\Omega_{ij}$, γ_{ij} , and ε_{ij} are respectively the coupling energy, broadening parameter, and energy difference associated with the states $|i\rangle$ and $|j\rangle$, k_B is the Boltzmann constant, and T_e represents the average electron temperature of the states. As we are dealing with a ‘‘closed’’ system, the diagonal elements of the DM must add up to 1, which enables us to eliminate ρ_{11} from Eqs. (3.2) and (3.3). Thus, we get

$$\dot{\rho}_{22} = C_2 - C_1\rho_{22} - C_2\rho_{33} + iaE_z(\rho_{23} - \rho_{23}^*) + D\frac{\partial^2 \rho_{22}}{\partial x^2}, \quad (3.5)$$

$$\dot{\rho}_{33} = \alpha_{13} + C_4\rho_{22} - C_5\rho_{33} + iaE_z(\rho_{23}^* - \rho_{23}) + D\frac{\partial^2 \rho_{33}}{\partial x^2}, \quad (3.6)$$

where $C_1 = \alpha_{12}(1 + \beta_{12}) + \tau_{23}^{-1} + \tau_{21}^{-1}$, $C_2 = \alpha_{12}\beta_{12}$, $C_4 = -\alpha_{13} + \tau_{23}^{-1}$, and $C_5 = \alpha_{13}(1 + \beta_{13}) + \tau_{31}^{-1}$.

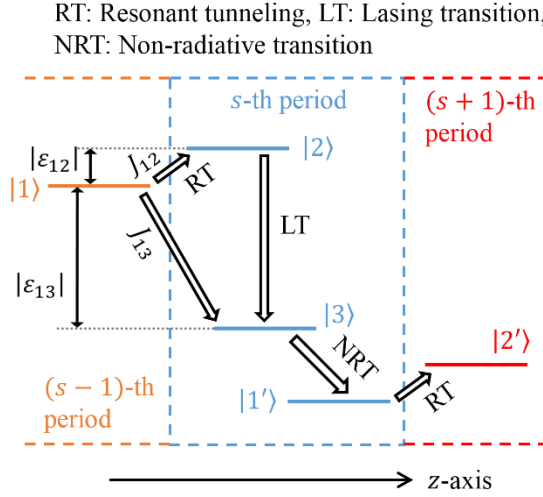


Figure 3.1: Schematic illustration of carrier transport through the QCL periods under an appropriate bias. Each period is assumed to have three energy levels.

Since our focus is to study single-mode instability, we take the field inside the cavity to be composed of a strong primary mode and two weak side modes with one chosen from each side of the primary mode. In our derivation, we treat the couplings up to the first order in the side modes, which is equivalent to ignoring the saturation of the side modes. Therefore, our theory is valid for lasing operation up to single-mode-instability boundary, i.e., up to the onset of single-mode instability. We expand the field and the elements of the DM in terms of SV amplitudes and rapidly varying exponential functions:

$$E_z = E_0(x,t)e^{-i\omega_0 t} + E_+(x,t)e^{-i\omega_+ t} + E_-(x,t)e^{-i\omega_- t} + \text{c.c.}, \quad (3.7)$$

$$\rho_{b=22,33} = \rho_{\text{dc},b}(x,t) + \rho_{\delta,b}(x,t)e^{-i\delta\omega t} + \text{c.c.}, \quad (3.8)$$

$$\rho_{23} = \eta_0(x,t)e^{-i\omega_0 t} + \eta_+(x,t)e^{-i\omega_+ t} + \eta_-(x,t)e^{-i\omega_- t}, \quad (3.9)$$

where ω_0 is the frequency of the primary mode, ω_{\pm} are the frequencies of the side modes and are expressed as $\omega_{\pm} = \omega_0 \pm \delta\omega$, and $\delta\omega$ is the side-mode detuning from the primary mode. We have assumed ω_+ and ω_- to be equally detuned from ω_0 because such phenomenon was observed in the experiment [12]. The subscript “dc” is used to denote that the corresponding quantity is the coefficient of the zero-frequency exponential function. ω_0 and ω_{\pm} are the oscillation frequencies and also known as the hot-cavity frequencies. Due to dispersion of the gain medium, these frequencies generally differ from the cold-cavity frequencies [35]. We assume that the FP cavity

is closed, i.e., the reflectivity of both the facets is unity. This assumption simplifies our analysis due to the fact that the eigenmodes of a closed cavity are well-defined and orthogonal to each other. Though our theory is derived by employing the closed-cavity assumption, it is, as well, applicable for QCLs with facets of non-unity but equal/nearly equal reflectivity, i.e., symmetric reflectivity [13]. However, it cannot predict instability in QCLs having facets with asymmetric reflectivity. Because the cavity is sharply resonant around its eigenmodes, we assume that the temporal and spatial variations of the field amplitudes $E_{l=0,+,-}(x,t)$ are separable [36]. So, we write $E_l(x,t) = Y_l(x)F_l(t)$, where the cavity eigenmode $Y_l(x)$ is given by $Y_l(x) = (1/\sqrt{2})[\exp(ik_l x) + \exp(-ik_l x)]$ and k_l is an allowed wavevector. The cold-cavity frequencies are related to wavevectors by $\Omega_l = k_l c/n(\Omega_l)$, where $n(\Omega_l)$ and c are the frequency-dependent background refractive index and the light velocity in free space, respectively. We assume that a cold-cavity mode of mode number N_{23} exists at the line center; putting it another way, we assume that the relation $N_{23} \pi/L = n(\omega_{23})\omega_{23}/c$ holds, where L is the length of the cavity. Thus, we write $k_{l=0,+,-}$ in terms of N_{23} as $k_l = (N_{23} + N_l)\pi/L$, where $N_{23} + N_l$ is the mode number for the l -th mode and N_l is the corresponding mode index (or mode offset). Now, plugging Eqs. (3.7)–(3.9) into Eqs. (3.4)–(3.6) and equating the terms that have the same argument for the exponential functions, we obtain a system of coupled PDEs as follows:

$$\dot{\rho}_{\text{dc},22} = C_2 - C_1 \rho_{\text{dc},22} - C_2 \rho_{\text{dc},33} + ia \left[(Y_0 F_0)^* \eta_0 - Y_0 F_0 \eta_0^* \right] + D \frac{\partial^2 \rho_{\text{dc},22}}{\partial x^2}, \quad (3.10)$$

$$\dot{\rho}_{\text{dc},33} = \alpha_{13} + C_4 \rho_{\text{dc},22} - C_5 \rho_{\text{dc},33} - ia \left[(Y_0 F_0)^* \eta_0 - Y_0 F_0 \eta_0^* \right] + D \frac{\partial^2 \rho_{\text{dc},33}}{\partial x^2}, \quad (3.11)$$

$$\dot{\eta}_0 = - \left[i(\omega_{23} - \omega_0) + \tau_{\parallel,23}^{-1} \right] \eta_0 + ia (Y_0 F_0 \rho_{\text{dc},22} - Y_0 F_0 \rho_{\text{dc},33}), \quad (3.12)$$

$$\dot{\rho}_{\delta,22} = -(C_1 - i\delta\omega) \rho_{\delta,22} - C_2 \rho_{\delta,33} + ia \left[(Y_- F_-)^* \eta_0 - Y_+ F_+ \eta_0^* + (Y_0 F_0)^* \eta_+ - Y_0 F_0 \eta_-^* \right], \quad (3.13)$$

$$\dot{\rho}_{\delta,33} = C_4 \rho_{\delta,22} - (C_5 - i\delta\omega) \rho_{\delta,33} - ia \left[(Y_- F_-)^* \eta_0 - Y_+ F_+ \eta_0^* + (Y_0 F_0)^* \eta_+ - Y_0 F_0 \eta_-^* \right], \quad (3.14)$$

$$\dot{\eta}_+ = -\left[i(\omega_{23} - \omega_+) + \tau_{\parallel,23}^{-1} \right] \eta_+ + ia \left(Y_0 F_0 \rho_{\delta,22} - Y_0 F_0 \rho_{\delta,33} + Y_+ F_+ \rho_{dc,22} - Y_+ F_+ \rho_{dc,33} \right), \quad (3.15)$$

and

$$\dot{\eta}_- = -\left[i(\omega_{23} - \omega_-) + \tau_{\parallel,23}^{-1} \right] \eta_- + ia \left(Y_0 F_0 \rho_{\delta,22}^* - Y_0 F_0 \rho_{\delta,33}^* + Y_- F_- \rho_{dc,22} - Y_- F_- \rho_{dc,33} \right). \quad (3.16)$$

As done in Refs. [21] and [31], we require the steady-state solution to these PDEs, which is achieved according to the following sequence. First, we make the time derivatives of these SV terms to zero. Since Eqs. (3.10)–(3.12) have terms containing SV amplitudes associated with the primary mode only, which is the consequence of our treatment of the couplings up to the first order in the side modes, we, then, proceed to solve these equations for $\rho_{dc,b=22,33}$ and η_0 . However, in order to get rid of the spatial derivatives, we need to know the form of the spatial variation of $\rho_{dc,b}$. Therefore, second, we drop the terms containing spatial derivatives in Eqs. (3.10)–(3.12) and solve these equations for $\rho_{dc,b}$. By keeping the terms up to second order in $E_0 (= Y_0 F_0)$, we find that $\rho_{dc,b}$ has the form $\rho_{dc,b} = G_b + H_b \cos(2k_0 x)$, where G_b and H_b are parameters free of spatial coordinate. Third, assuming that G_b and H_b are unknown parameters, we put the aforementioned form of $\rho_{dc,b}$ in Eqs. (3.10)–(3.12) and equate the coefficients of $\cos(2k_0 x)$ terms as well as $\cos(2k_0 x)$ -free terms. Contrary to what we have done in the second step, in this step, we consider the terms containing the spatial derivatives in Eqs. (3.10)–(3.12). Thus, we find the expressions of G_b , H_b , and η_0 . Finally, we put the expressions of $\rho_{dc,b}$ and η_0 in Eqs. (3.13)–(3.16) and solve these equations for the SV amplitudes associated with the side modes. Thus, following these steps, we arrive at the expressions below:

$$W = \rho_{dc,22} - \rho_{dc,33} = \left[1 - \left(\frac{C_1 + C_2 + C_5 - C_4}{C_1 C_5 + C_2 C_4} + \frac{(C_1 + C_2 + C_5 - C_4 + 8Dk_0^2) \cos(2k_0 x)}{(C_1 + 4Dk_0^2)(C_5 + 4Dk_0^2) + C_2 C_4} \right) \frac{2a^2 \tau_{\parallel,23}}{1 + (\omega_{23} - \omega_0)^2 \tau_{\parallel,23}^2} |F_0|^2 \right] W_{\text{eq}}, \quad (3.17)$$

$$\eta_0 = \frac{i a \tau_{\parallel,23} W}{1 + i(\omega_{23} - \omega_0) \tau_{\parallel,23}} Y_0 F_0, \quad (3.18)$$

$$\eta_+ = -\frac{\varepsilon_0}{N \Gamma a \hbar} \left[\left(\chi_+^L + \chi_+^{\text{NL}} |Y_0 F_0|^2 \right) Y_+ F_+ + \chi_{+-}^{\text{NL}} (Y_0 F_0)^2 Y_-^* F_-^* \right], \quad (3.19)$$

$$\eta_- = -\frac{\varepsilon_0}{N \Gamma a \hbar} \left[\left(\chi_-^L + \chi_-^{\text{NL}} |Y_0 F_0|^2 \right) Y_- F_- + \chi_{-+}^{\text{NL}} (Y_0 F_0)^2 Y_+^* F_+^* \right], \quad (3.20)$$

$$\chi_{b1=+,-}^L = -\frac{i N \Gamma a^2 \hbar \tau_{\parallel,23} W}{\varepsilon_0} \overline{\chi_{b1}^L}, \quad \chi_{b2=+,+,-,-,+}^{\text{NL}} = \frac{2i N \Gamma a^4 \hbar \tau_{\parallel,23}^2 W_{\text{eq}}}{\varepsilon_0 \left[1 + (\omega_{23} - \omega_0)^2 \tau_{\parallel,23}^2 \right]} \overline{\chi_{b2}^{\text{NL}}}, \quad (3.21)$$

$$\overline{\chi_+^L} = \frac{1}{1 + i(\omega_{23} - \omega_0 - \delta\omega) \tau_{\parallel,23}}, \quad (3.22)$$

$$\overline{\chi_+^{\text{NL}}} = \frac{\left[1 + i(\omega_{23} - \omega_0) \tau_{\parallel,23} \right] (1 - i\delta\omega \tau_{\parallel,23} / 2) (C_1 + C_2 + C_5 - C_4 - 2i\delta\omega)}{\left[1 + i(\omega_{23} - \omega_0 - \delta\omega) \tau_{\parallel,23} \right]^2 \left[(C_5 - i\delta\omega)(C_1 - i\delta\omega) + C_2 C_4 \right]}, \quad (3.23)$$

and

$$\overline{\chi_{+-}^{\text{NL}}} = \frac{\left[1 - i(\omega_{23} - \omega_0) \tau_{\parallel,23} \right] (1 - i\delta\omega \tau_{\parallel,23} / 2) (C_1 + C_2 + C_5 - C_4 - 2i\delta\omega)}{\left[1 + i(\omega_{23} - \omega_0 - \delta\omega) \tau_{\parallel,23} \right] \left[1 - i(\omega_{23} - \omega_0 + \delta\omega) \tau_{\parallel,23} \right] \left[(C_5 - i\delta\omega)(C_1 - i\delta\omega) + C_2 C_4 \right]}, \quad (3.24)$$

where W_{eq} is the population inversion that would occur in the absence of lasing and is given by $W_{\text{eq}} = (C_2 C_5 - \alpha_{13} C_2 - \alpha_{13} C_1 - C_2 C_4) / (C_1 C_5 + C_2 C_4)$, ε_0 is the vacuum permittivity, N is the free electron concentration, Γ represents the overlap factor between the optical field and the active region, and χ_{b1}^L and χ_{b2}^{NL} are the linear and non-linear susceptibilities [13], respectively. The scaled susceptibilities $\overline{\chi_{b1}^L}$ and $\overline{\chi_{b2}^{\text{NL}}}$ are introduced in order to simplify the final expressions [see Eqs. (3.37) and (3.38) below]. In Eqs. (3.17), (3.23), and (3.24), we keep terms up to second order in E_0 , and the underlying assumption is that the central-mode field remains much weaker than the saturation field throughout the single-mode operation, i.e., $|E_0|^2 \ll E_{\text{sat}}^2$, where

$$E_{\text{sat}}^2 = \frac{C_1 C_5 + C_2 C_4}{C_1 + C_2 + C_5 - C_4} \frac{1 + (\omega_{23} - \omega_0)^2 \tau_{\parallel,23}^2}{2a^2 \tau_{\parallel,23}}. \text{ Furthermore, the expressions of } \overline{\chi_-^L}, \overline{\chi_-^{\text{NL}}}, \text{ and } \overline{\chi_{-+}^{\text{NL}}}$$

can be found by simply replacing $\delta\omega$ with $-\delta\omega$ in Eqs. (3.22)–(3.24), respectively.

Unlike Refs. [28] and [29], which considered the diffusion of ρ_{23} (coherence diffusion), we have not taken this diffusion into account. This diffusion can be included in our analysis by adding an extra term $D \frac{\partial^2 \rho_{23}}{\partial x^2}$ to Eq. (3.4). As shown in Eqs. (3.8) and (3.9) in Ref. [29], inclusion of the coherence diffusion converts $\tau_{\parallel,23}^{-1}$ into two new rates, namely relaxation rate of the coherence grating $\tau_{\parallel,23,g}^{-1} = (\tau_{\parallel,23}^{-1} + 9Dk_0^2)$ and effective carrier dephasing rate in the presence of diffusion $\tau_{\parallel,23,\text{eff}}^{-1} = (\tau_{\parallel,23}^{-1} + Dk_0^2)$. Let us compare the term $9Dk_0^2$ with $\tau_{\parallel,23}^{-1}$ for mid-IR QCLs operating in the different wavelength regions. For a QCL that lases around $\lambda_0 = 3.5 \mu\text{m}$, if we take $\tau_{\parallel,23} = 43 \text{ fs}$ [13], $D = 77 \text{ cm}^2/\text{s}$ [20], and $n(\omega_0) = 3.25$ [13], we find that $\tau_{\parallel,23}^{-1}/9Dk_0^2 \approx 10$. Furthermore, for a QCL operating around $\lambda_0 = 10 \mu\text{m}$, we find by using $\tau_{\parallel,23} = 81 \text{ fs}$ [13] and $n(\omega_0) = 3.43$ [13] that $\tau_{\parallel,23}^{-1}/9Dk_0^2 \approx 38$. For mid-IR QCLs operating in the longer wavelength region, i.e., longer than $10 \mu\text{m}$, this ratio will be similar to or higher than the above values. Since the term $9Dk_0^2$ is, at least, an order of magnitude smaller than $\tau_{\parallel,23}^{-1}$, the rates $\tau_{\parallel,23,g}^{-1}$ and $\tau_{\parallel,23,\text{eff}}^{-1}$ will be close to $\tau_{\parallel,23}^{-1}$ for mid-IR QCLs operating with $\lambda_0 > \sim 3.5 \mu\text{m}$. So, we expect that our theory, where we have implicitly taken these two rates to be equal to $\tau_{\parallel,23}^{-1}$, will work well for mid-IR QCLs operating in the region $\lambda_0 > \sim 3.5 \mu\text{m}$. However, for shorter-wavelength QCLs (i.e., $\lambda_0 < \sim 3.5 \mu\text{m}$), the term $9Dk_0^2$ could be comparable to $\tau_{\parallel,23}^{-1}$, and thus taking coherence diffusion into account might be necessary.

To get an EoM for each of the modes, we use Maxwell's equation of the following form

$$\frac{\partial^2 E_z}{\partial x^2} - \frac{1}{c^2} \frac{\partial^2 E_z}{\partial t^2} = \frac{1}{\varepsilon_0 c^2} \frac{\partial^2 P}{\partial t^2}, \quad (3.25)$$

where total polarization $P = P_{\text{back}} + P_{\text{NL}}$, polarization of the background host medium is given by

$$P_{\text{back}} = \varepsilon_0 \left[\sum_{l=0,+,-} \chi_{\text{back}}(\omega_l) Y_l F_l e^{-i\omega_l t} \right] + \text{c.c.}, \quad \chi_{\text{back}}(\omega_l) \text{ represents the susceptibility of the host}$$

medium, and the nonlinear polarization due to the three-level QCL periods is given by $P_{\text{NL}} = -N\Gamma a\hbar(\rho_{23} + \rho_{23}^*)$. The term representing the total loss will be added later. Now, after plugging the expansions of E_z and ρ_{23} into Eq. (3.25), by keeping the terms containing only positive frequencies, by making the slowly-varying envelope approximations (i.e., by ignoring the second time-derivative of F_l and the first and second time-derivatives of η_l), and by using the relations $\frac{\partial^2 Y_l}{\partial x^2} = -k_l^2 Y_l$ and $[n(\omega_l)]^2 = 1 + \chi_{\text{back}}(\omega_l)$, we get

$$\sum_{l=0,+,-} \left\{ \frac{[n(\omega_l)]^2 \omega_l^2}{c^2} - k_l^2 \right\} Y_l F_l e^{-i\omega_l t} + \frac{2i}{c^2} \sum_{l=0,+,-} [n(\omega_l)]^2 \omega_l Y_l \dot{F}_l e^{-i\omega_l t} = \frac{N\Gamma a\hbar}{\epsilon_0 c^2} \sum_{l=0,+,-} \omega_l^2 \eta_l e^{-i\omega_l t}. \quad (3.26)$$

If we put the expression of η_0 in Eq. (3.26), project this equation onto the eigenmode $Y_0(x)$, and equate the terms oscillating at frequency ω_0 , we get the EoM for the central mode

$$\begin{aligned} \dot{F}_0 = & -\frac{1}{2} \frac{l_d c}{n(\omega_0)} F_0 + \frac{i}{2} \left\{ \omega_0 - \frac{k_0^2 c^2}{[n(\omega_0)]^2 \omega_0} \right\} F_0 + \frac{N\Gamma a^2 \hbar \omega_0 \tau_{\parallel,23}}{2\epsilon_0 [n(\omega_0)]^2 [1 + i(\omega_{23} - \omega_0) \tau_{\parallel,23}]} \\ & \times \left[1 - (A + B/2) \frac{2a^2 \tau_{\parallel,23}}{1 + (\omega_{23} - \omega_0)^2 \tau_{\parallel,23}^2} |F_0|^2 \right] W_{\text{eq}} F_0. \end{aligned} \quad (3.27)$$

Here, $A = \frac{C_1 + C_2 + C_5 - C_4}{C_1 C_5 + C_2 C_4}$ and $B = \frac{C_1 + C_2 + C_5 - C_4 + 8Dk_0^2}{(C_1 + 4Dk_0^2)(C_5 + 4Dk_0^2) + C_2 C_4}$. We assume that all three

modes experience the same intensity loss per unit distance l_d [37]. For a mode l , intensity loss per unit distance l_d can be converted to intensity loss per unit time $l_{s,l}$ by using $l_{s,l=0,+,-} = l_d c / n(\omega_l)$ [13]. Thus, the first term on the right-hand side (RHS) of Eq. (3.27), which has been added, denotes the amplitude loss experienced by the central mode per unit time (i.e., $\frac{1}{2} l_{s,0}$). The second term on the RHS arises due to the fact that the hot-cavity frequency is not necessarily equal to a cold-cavity frequency. The third term originates from η_0 , thus representing the response of the three-level system to the primary-mode light.

Now, we assume the steady-state operation for the primary mode, setting $\dot{F}_0 = 0$ in Eq. (3.27). First, we equate the real part of the RHS of Eq. (3.27) to zero [$\text{Re}(\text{RHS}) = 0$]. It means applying the ‘‘gain condition’’ on the central mode, i.e., for F_0 to become nonzero, W_{eq} has to exceed a threshold value W_{th} . The expression for W_{th} can be found by setting $F_0 = 0$ in $\text{Re}(\text{RHS}) = 0$, which reads

$$W_{\text{th}} = \frac{l_d c \varepsilon_0 n(\omega_0) \left[1 + (\omega_{23} - \omega_0)^2 \tau_{\parallel,23}^2 \right]}{N \Gamma a^2 \hbar \omega_0 \tau_{\parallel,23}}. \quad (3.28)$$

Now, by introducing a parameter called pumping parameter $p = W_{\text{eq}}/W_{\text{th}}$ in $\text{Re}(\text{RHS}) = 0$, we get the following expression for the primary-mode amplitude

$$|F_0|^2 = \frac{1 + (\omega_{23} - \omega_0)^2 \tau_{\parallel,23}^2}{2a^2 \tau_{\parallel,23}} \frac{(p-1)/p}{A + B/2}. \quad (3.29)$$

Next, we equate the imaginary part of the RHS of Eq. (3.27) to zero, which means ensuring that the primary-mode frequency is allowed in the cavity (in other words, satisfying the cavity-resonance condition). Thus, we obtain the following expression for the primary-mode frequency

$$\omega_0 = \frac{\omega_{23} \left\{ l_d c \tau_{\parallel,23} + \sqrt{(l_d c \tau_{\parallel,23})^2 + 4 \left[n(\omega_0) + l_d c \tau_{\parallel,23} \right] \frac{1}{n(\omega_0)} \left[n(\omega_{23}) + \frac{N_0 \pi c}{L \omega_{23}} \right]^2} \right\}}{2 \left[n(\omega_0) + l_d c \tau_{\parallel,23} \right]}. \quad (3.30)$$

We note that, in the absence of the third term on the RHS of Eq. (3.27), i.e., in the absence of the active medium, equating the imaginary part to zero would result in

$$\omega_0 = k_0 c / n(\omega_0) = \frac{(N_{23} + N_0) \pi}{L} \frac{c}{n(\omega_0)},$$

which means that ω_0 would be a cold-cavity frequency corresponding to N_0 . However, ω_0 shifts from the cold-cavity frequencies in the presence of the active medium and is now given by Eq. (3.30). We can also say that Eq. (3.30) generates a set of hot-cavity frequencies corresponding to different values of N_0 . In the next section, we will explain how the primary mode chooses a particular value of ω_0 (hence N_0) for lasing.

Now, to obtain the EoMs for the side modes, we put the expressions of η_{\pm} in Eq. (3.26), project it onto the eigenmodes $Y_{\pm}(x)$, and equate the terms oscillating at ω_{\pm} . Thus, we get

$$\dot{F}_+ = S_+ F_+ + C_+ F_-^*, \quad (3.31)$$

$$\dot{F}_-^* = S_-^* F_-^* + C_-^* F_+, \quad (3.32)$$

where S_+ and C_+ are given by

$$\begin{aligned} S_+ = & -\frac{1}{2} \frac{l_d c}{n(\omega_+)} + \frac{i}{2\omega_+} \left[\omega_+^2 - \left(\Omega_+ \frac{n(\Omega_+)}{n(\omega_+)} \right)^2 \right] + \frac{l_{s,0}}{2} \frac{\omega_+}{\omega_0} \left(\frac{n(\omega_0)}{n(\omega_+)} \right)^2 \left[1 + (\omega_{23} - \omega_0)^2 \tau_{\parallel,23}^2 \right] \overline{\chi_+^L} \\ & \times \left(1 + \frac{B(p-1)/2}{A+B/2} \right) - \frac{l_{s,0}}{2} \frac{\omega_+}{\omega_0} \left(\frac{n(\omega_0)}{n(\omega_+)} \right)^2 \left[1 + (\omega_{23} - \omega_0)^2 \tau_{\parallel,23}^2 \right] \overline{\chi_+^{\text{NL}}} \frac{p-1}{A+B/2} \end{aligned} \quad (3.33)$$

and

$$C_+ = -\frac{l_{s,0}}{2} \frac{(\omega_0 + \delta\omega)^2}{\omega_0 \omega_+} \left(\frac{n(\omega_0)}{n(\omega_+)} \right)^2 \left[1 + (\omega_{23} - \omega_0)^2 \tau_{\parallel,23}^2 \right] \overline{\chi_{+-}^{\text{NL}}} \frac{p-1}{A+B/2} \frac{1}{2} e^{i\theta}. \quad (3.34)$$

Here, $\theta = 2 \arg(F_0)$. S_- and C_- can be found from Eqs. (3.33) and (3.34), respectively, by replacing all the plus subscripts with the minus subscripts and vice versa. Additionally, for C_- , the term $\omega_0 + \delta\omega$ has to be replaced with $\omega_0 - \delta\omega$ in Eq. (3.34). Let us focus briefly on each term in Eqs. (3.33) and (3.34). The first term in the expression of S_+ represents the amplitude loss experienced by the $+$ mode per unit time. The second term arises due to the frequency difference between the hot- and cold-cavity modes. In the absence of the active medium, ω_+ would be equal to Ω_+ . However, in its presence, ω_+ (and ω_-) will deviate from the cold-cavity value so as to ensure that the imaginary part of the gain that the side modes experience vanishes. The third term is the linear contribution of the dipoles to the motion of the $+$ mode—linear in the sense that this term exists even when $F_0 = 0$. The fourth term in Eq. (3.33) and C_+ in Eq. (3.34) represent the non-linear (or coherent) contributions to the $+$ mode; they result from the interactions between

the primary and + modes and between the primary and - modes, respectively, as can be seen from Eq. (3.19). The phases of the primary and side modes are assumed to be matched, i.e., $2k_0 - k_+ - k_- = 0$. As a result, the overlap integral $(1/L) \int_0^L Y_0^2 Y_- Y_+ dx$ becomes 1/2, and this is denoted by an extra 1/2 factor in Eq. (3.34). We note that a phase mismatch between the modes would make both C_+ and C_- zero and thus would decouple Eqs. (3.31) and (3.32). Finally, though C_+ (and C_-) depends on θ , the gain of the side modes is independent of θ , as we will see next.

We write the solutions of Eqs. (3.31) and (3.32) in the following form:

$$F_+ = D_+ e^{g_a t} \quad \text{and} \quad F_-^* = D_- e^{g_a t}, \quad (3.35)$$

where g_a represents the net amplitude gain of the side modes. By plugging Eq. (3.35) into the respective EoMs, we get the following expression for the normalized net intensity gain:

$$g_{m=1,2} = \frac{2g_a}{l_{s,0}} = \frac{S_+ + S_-^*}{l_{s,0}} \pm \sqrt{\left(\frac{S_+ - S_-^*}{l_{s,0}}\right)^2 + \frac{4C_+ C_-^*}{l_{s,0}^2}}, \quad (3.36)$$

where

$$\begin{aligned} \frac{S_+ \pm S_-^*}{l_{s,0}} &= \frac{n(\omega_0)}{2} \left(-\frac{1}{n(\omega_+)} \mp \frac{1}{n(\omega_-)} \right) \\ &+ \frac{i}{2} \frac{n(\omega_0)}{l_d c} \left\{ \omega_+ \mp \omega_- - \frac{k_+^2 c^2}{[n(\omega_+)]^2 \omega_+} \pm \frac{k_-^2 c^2}{[n(\omega_-)]^2 \omega_-} \right\} + \frac{[n(\omega_0)]^2 [1 + (\omega_{23} - \omega_0)^2 \tau_{\parallel,23}^2]}{2\omega_0} \\ &\times \left[\left(1 + \frac{B(p-1)/2}{A+B/2} \right) \left\{ \frac{\omega_+ \overline{\chi_+^L}}{[n(\omega_+)]^2} \pm \frac{\omega_- \overline{\chi_-^L}}{[n(\omega_-)]^2} \right\} - \left(\frac{p-1}{A+B/2} \right) \left\{ \frac{\omega_+ \overline{\chi_+^{\text{NL}}}}{[n(\omega_+)]^2} \pm \frac{\omega_- \overline{\chi_-^{\text{NL}}}}{[n(\omega_-)]^2} \right\} \right] \end{aligned} \quad (3.37)$$

and

$$\frac{4C_+ C_-^*}{l_{s,0}^2} = \left\{ \frac{[n(\omega_0)]^2 \sqrt{\omega_+ \omega_-}}{2n(\omega_+)n(\omega_-)\omega_0} [1 + (\omega_{23} - \omega_0)^2 \tau_{\parallel,23}^2] \frac{p-1}{A+B/2} \right\}^2 \frac{\overline{\chi_+^{\text{NL}}} \overline{\chi_-^{\text{NL}}}}{\chi_+^{\text{NL}} \chi_-^{\text{NL}}}. \quad (3.38)$$

Here, g_1 (g_2) corresponds to the expression with the positive (negative) square root. In general,

there exists a threshold for pumping, p_{inst} , below which no values of the side-mode detuning will simultaneously satisfy the conditions

$$\text{Re}(g_m) > 0 \text{ and } \text{Im}(g_m) = 0. \quad (3.39)$$

Hence, for $p < p_{\text{inst}}$, the laser remains stable, emitting only the primary-mode light. (The subscript ‘‘inst’’ denotes that the corresponding quantity is a value at the onset of instability.) When p increases to p_{inst} , usually a value of the detuning, namely $\delta\omega_{\text{inst}}$, can be found that satisfy both of these conditions. In this case, we say that the laser becomes unstable at a pumping p_{inst} and that the side modes will oscillate at $\omega_{+, \text{inst}}$ and $\omega_{-, \text{inst}}$ frequencies at the onset of instability. These two conditions in Eq. (3.39) together constitute necessary and sufficient conditions for a laser to become unstable [32]. According to Ref. [13], side modes corresponding to one of the two solutions in Eq. (3.36) behave like an FM wave, i.e., the relative phase of the side modes $\varphi = \arg(F_-^*) - \arg(F_+) + 2\arg(F_0) \approx -\pi$ and the ratio between the side-mode amplitudes $|F_-^*/F_+| \approx 1$, and side modes corresponding to the other solution have the characteristic of an AM wave, i.e., $\varphi \approx 0$ and $|F_-^*/F_+| \approx 1$. However, the side modes corresponding to g_1 and g_2 may not always behave like FM/AM waves, especially when the GVD is high, as we will see in the next section. We can determine the relative phase and the amplitude ratio, and thus understand the nature, of the side modes by using

$$\varphi_{m=1,2} = \arg\left(\frac{g_m - 2S_+/l_{s,0}}{2C_+ e^{-i\theta}/l_{s,0}}\right) \text{ and } \left|\frac{F_-^*}{F_+}\right|_{m=1,2} = \left|\frac{g_m - 2S_+/l_{s,0}}{2C_+ e^{-i\theta}/l_{s,0}}\right|. \quad (3.40)$$

In Appendix A, we show that the expressions derived in this section can be reduced to the corresponding expressions for a two-level system. We also show that the reduced expressions agree with those in Ref. [13].

3.4 Results and discussion

The QCL that we choose for the simulations in this chapter is a typical mid-IR laser with a short gain recovery time, and its parameters are given in Table 3.1. The frequency dependence of refractive index gives rise to GVD, and the second derivative of the wavevector with respect to

frequency, i.e., $\alpha = d^2k_l/d\Omega_l^2$, is a measure of GVD. For QCLs, GVD mainly originates from the material and waveguide. Using the relation between k_l and Ω_l and then ignoring the second derivative of $n(\Omega_l)$ with respect to Ω_l , we get $\alpha = (2/c)dn/d\Omega$, which, in turn, leads to the following expression of the refractive index [12]:

$$n(\Omega_l) = n(\omega_{23}) + \frac{c}{2} \alpha (\Omega_l - \omega_{23}). \quad (3.41)$$

At first, we focus on the following issue regarding the central-mode detuning: How can we determine the detuning of the primary-mode frequency from the line-center frequency ω_{23} ? Primary-mode frequency, ω_0 , which is given by Eq. (3.30), depends on the index N_0 . A zero value of N_0 results in $\omega_0 = \omega_{23}$, and the more deviation N_0 makes from zero, the more deviation ω_0 undergoes from the line-center frequency. Since W_{th} depends on ω_0 , as shown in Eq. (3.28), W_{th} is also a function of N_0 . The characteristic of W_{th} versus N_0 relation is that W_{th} has a minimum point at $N_0 = N_{0,min}$. Now, starting from a point below lasing threshold, if the pumping level of a laser is gradually increased, the lasing will, or is likely to, commence when W_{eq} becomes equal to the value of W_{th} at the minimum point. Consequently, the primary mode will lase at $\omega_{0,min}$, where $\omega_{0,min}$ is the value of ω_0 at $N_{0,min}$.

Table 3.1: Parameters of the mid-IR QCL used for simulations in this chapter [20,38]

Parameters related to $1\rangle \rightarrow 2\rangle$			
and $1\rangle \rightarrow 3\rangle$ electron tunneling		Electron scattering rates	Values
		Values	
$ 1\rangle \leftrightarrow 2\rangle$ coupling energy, $\hbar\Omega_{12}$	1.06 meV	$ 2\rangle \rightarrow 3\rangle$ scattering rate, τ_{23}^{-1}	$(1 \text{ ps})^{-1}$

$ 1\rangle \leftrightarrow 2\rangle$ broadening parameter,		$ 2\rangle \rightarrow 1'\rangle$	
γ_{12}	6.58 meV	scattering rate,	
		$\tau_{21'}^{-1}$	$(3 \text{ ps})^{-1}$
$ 1\rangle \leftrightarrow 3\rangle$ coupling energy, $\hbar\Omega_{13}$	0 meV	$ 3\rangle \rightarrow 1'\rangle$	
Average electron temperature (assumed the same for all states),		scattering rate,	
T_e	300 K	$\tau_{31'}^{-1}$	$(0.1 \text{ ps})^{-1}$
<hr/>			
		Parameters related to laser structure	
Optical parameters	Values		Values
	$\sim 2\pi \times 48.36 \text{ THz}$	Cavity length,	
Line-center frequency, ω_{23}	$(N_{23} = 3194)$	L	3 mm
Background refractive index at ω_{23} , $n(\omega_{23})$	3.3	Free electron concentration, N	$\sim 1.38 \times 10^{16} \text{ cm}^{-3}$
Overlap factor between the optical field and the active region, Γ	1	Diffusion coefficient, D	$77 \text{ cm}^2/\text{s}$
Dipole matrix element, z_{23}	2 nm		
Intensity loss per unit distance, l_d	$2 \times 11.16 \text{ cm}^{-1}$ (mirror loss included)		

The parameter $N_{0,\min}$ may not be zero; its deviation from zero, i.e., the detuning of the primary-mode frequency $\omega_{0,\min}$ from ω_{23} , depends on GVD, ω_{23} , and $\tau_{\parallel,23}$, as described in Eq. (3.28). In Fig. 3.2(a), we plot the primary-mode detuning as a function of $\tau_{\parallel,23}$ for a QCL with

zero GVD. The absolute value of the detuning increases with decreasing $\tau_{\parallel,23}$. Figure 3.2(b) shows how the detuning changes with GVD for a QCL having $\tau_{\parallel,23} = 0.05$ ps. In this case, the absolute value of the detuning becomes zero at $\alpha = 70000$ fs²/mm and increases as α moves further away from this point.

Let us explain the issue of central-mode detuning in a different way. Equation (3.28) can be written in the following form

$$\frac{(ez_{23})^2 \omega_0 \Gamma N W_{\text{th}}}{c \varepsilon_0 n(\omega_0)} \frac{\gamma_{23}}{\left[\gamma_{23}^2 + (\hbar \omega_{23} - \hbar \omega_0)^2 \right]} = l_d, \quad (3.42)$$

where we have written the dephasing time $\tau_{\parallel,23}$ in terms of the broadening parameter γ_{23} by using $\gamma_{23} = \hbar \tau_{\parallel,23}^{-1}$ (see Eq. (4.9.54) in Ref. [20]). The left-hand side of Eq. (3.42) represents the familiar expression of the intersubband gain experienced by a light of frequency ω_0 (see Eq. (4.4.21) in Ref. [20] and Eq. (52) in Ref. [39]). Equation (3.42) indicates that W_{th} will be minimum at a value of ω_0 where the peak of the intersubband gain occurs. We have found before that W_{th} becomes minimum at $\omega_0 = \omega_{0,\text{min}}$. Therefore, the intersubband gain peaks at $\omega_0 = \omega_{0,\text{min}}$ as well, not at $\omega_0 = \omega_{23}$. The detuning of the peak gain frequency ($\omega_{0,\text{min}}$) from ω_{23} depends on the broadening parameter γ_{23} (i.e., $\tau_{\parallel,23}$), on the shape of $n(\omega_0)$ (i.e., GVD), and on ω_{23} . Specifically, Fig. 3.2(a) shows that the peak gain frequency moves further away from the line-center frequency with increasing broadening. In summary, by taking the primary mode to lase at a frequency that minimizes W_{th} , we actually select for the primary mode a frequency where the gain peak occurs.

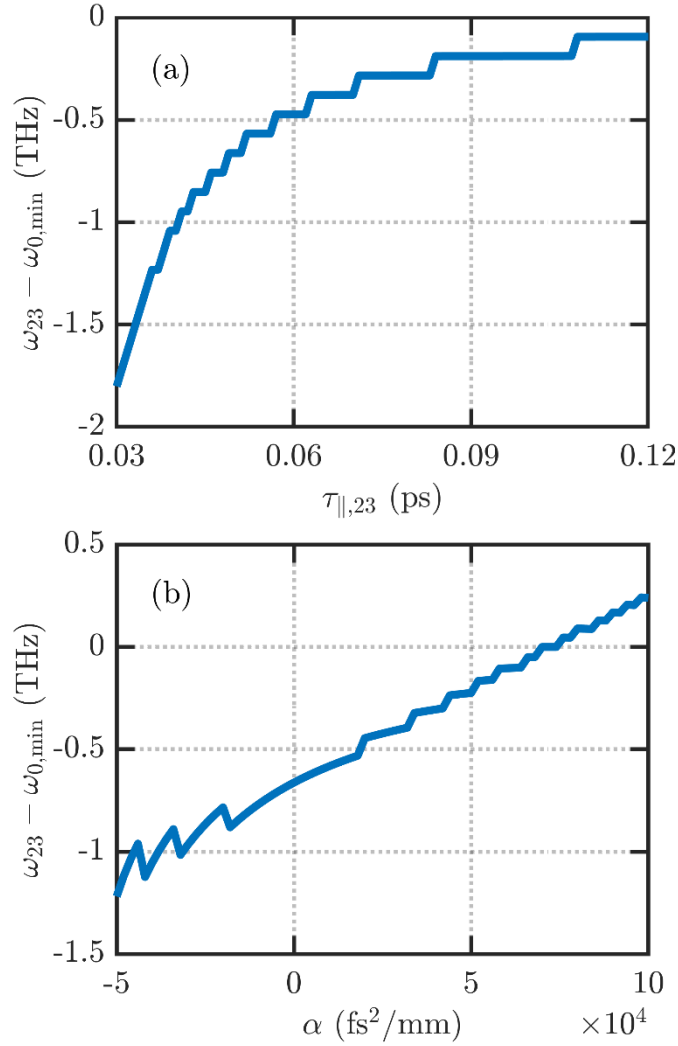


Figure 3.2: Detuning of the central-mode frequency from the line-center frequency (a) as a function of dephasing time and (b) as a function of GVD. In (a), GVD is taken to be zero, and in (b), the dephasing time is taken to be 0.05 ps. Other parameters are taken from Table 3.1.

Next, we discuss in detail how we determine instability and study the equations describing the gain, relative phase, amplitude ratio of the side modes. Since we assume that the central and side modes are phase-matched, in other words, k_+ and k_- are equidistant from the primary-mode wavevector $k_{0,\min} = (N_{23} + N_{0,\min})\pi/L$, we rewrite $k_{\pm} = (N_{23} + N_{0,\min} \pm N_{\text{side}})\pi/L$, where N_{side} is the side-mode index and is a positive integer (we can say that the side modes are situated N_{side} modes away from the central mode). Therefore, Eq. (3.36) has three independent variables, i.e., ε_{12} , $\delta\omega$, and N_{side} . We note that, in our three-level model, p is determined by the energy gap

ε_{12} : p increases as $|\varepsilon_{12}|$ decreases and vice versa. After determining the primary-mode frequency $\omega_{0,\min}$, we proceed to determine the onset of instability according to the following sequence. First, for a value of the pumping p , by using the second condition (cavity-resonance condition) in Eq. (3.39), we get a pool of allowed values of $\delta\omega$ (i.e., a pool of side-mode frequencies that are allowed to oscillate); each value of N_{side} produces an allowed value of $\delta\omega$. In the presence of an active medium, these allowed side-mode frequencies ($\omega_{0,\min} \pm$ allowed values of $\delta\omega$), not the cold-cavity frequencies, represent the new resonant frequencies of the cavity. These allowed frequencies can also be called hot-cavity frequencies corresponding to different values of N_{side} . Second, we filter this pool by using the first condition in Eq. (3.39) that checks whether the side modes at these allowed frequencies are able to overcome the total loss. For small pumping levels, no side modes from the pool will satisfy the first condition. Therefore, third, we slowly increase the pumping level and repeat the previous two steps. When the pumping level reaches the instability threshold p_{inst} , a value from the pool, $\delta\omega_{\text{inst}}$, will satisfy the first condition, which marks the onset of instability. The corresponding side-mode index is labeled as $N_{\text{side,inst}}$. Thus, we say that, when the laser becomes unstable, the side modes at frequencies $\omega_{\pm,\text{inst}} = \omega_{0,\min} \pm \delta\omega_{\text{inst}}$ will oscillate.

For a QCL having $\tau_{\parallel,23} = 0.12$ ps and zero GVD (other parameters listed in Table 3.1), we find that the central mode lases at $\sim 2\pi \times 48.38$ THz and that a pumping of ~ 1.23 (p_{inst}) makes the laser unstable, resulting in an oscillation of the side modes of index 13 ($N_{\text{side,inst}}$) at frequencies that are ~ 1.23 THz ($\delta\omega_{\text{inst}}$) away from the central-mode frequency. This is a harmonic instability since $N_{\text{side,inst}}$ is greater than 1. In Fig. 3.3, we show the real and imaginary parts of g_1 and g_2 , relative phases φ_1 and φ_2 , and side-mode amplitude ratios corresponding to $p \approx 1.23$ for this QCL. Allowed values of $\delta\omega$ are used to plot these graphs, which is denoted by $\text{Im}(g_{1,2}) \approx 0$ in Fig. 3.3(b). Figure 3.3(a) shows that the real parts of $g_{1,2}$ meet near 3.87 THz. Moreover, the plots

of $\varphi_{1,2}$ in Fig. 3.3(b) indicate that, in the region on the left side of the meeting point of $\text{Re}(g_{1,2})$, the values of φ_1 are close to $-\pi$ and those of φ_2 are close to 0. The ratios $|F_-^*/F_+|_{1,2}$ are close to 1 as well [Fig. 3.3(c)]. Therefore, in this region, side modes corresponding to g_1 (g_2) show the characteristic of an FM (AM) wave. However, their behaviors change in the region on the right side of the meeting point of $\text{Re}(g_{1,2})$. Because φ_1 and φ_2 are now reasonably close to 0 and $-\pi$, respectively, and the amplitude ratios are reasonably close to 1, g_1 -side modes and g_2 -side modes in this region behave like an AM and FM waves, respectively. The solid circles in Fig. 3.3 denote the onset-of-instability values, showing that the laser is likely to emit an FM-like light after being unstable.

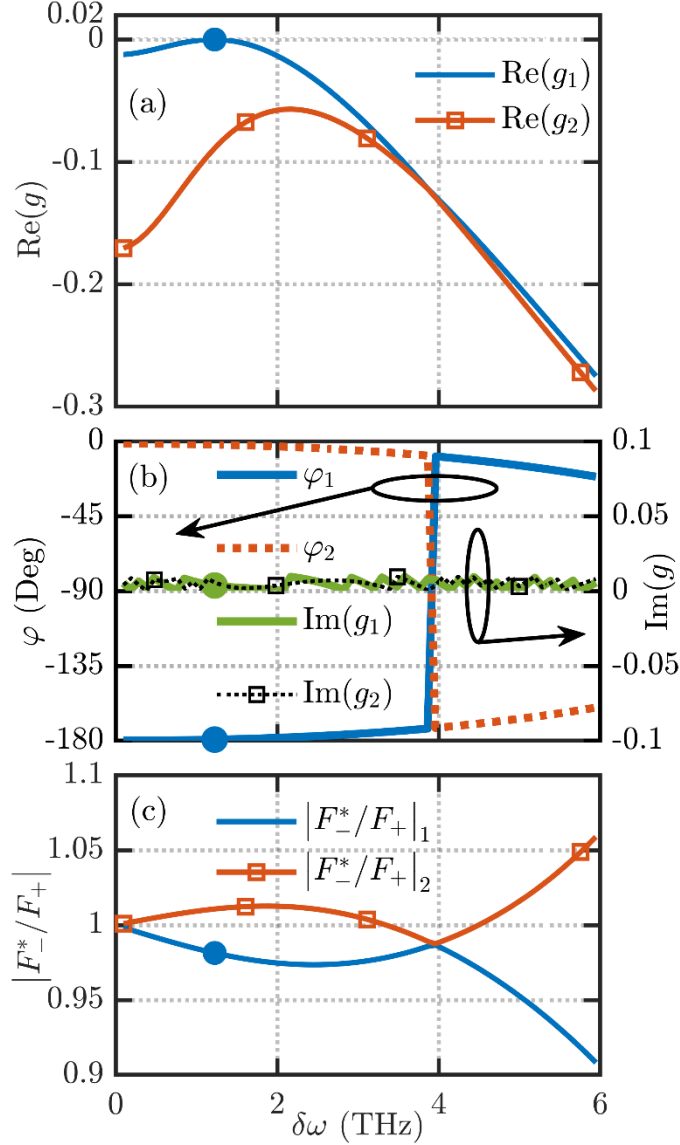


Figure 3.3: (a) Real parts and (b) imaginary parts of the normalized net intensity gains, relative phases of the side modes, and (c) side-mode amplitude ratios for a QCL with $\tau_{||,23} = 0.12$ ps and zero GVD. The QCL is pumped to its instability threshold, i.e., $p \approx 1.23$.

Now that we have discussed the instability determination procedure, we discuss the importance of considering central-mode detuning phenomenon in the theory. First, we choose a QCL with a dephasing time of 0.06 ps, which corresponds to a full-width-half-maximum (FWHM) gain broadening of ~ 22 meV. A similar broadening was reported in Ref. [40] for a mid-IR QCL with the two-phonon resonance design. As shown in Fig. 3.2(a), the absolute value of the detuning of the primary-mode frequency from ω_{23} is ~ 0.47 THz. By considering the detuning, we find

that the laser becomes unstable at a pumping of ~ 1.08 , and the side modes that are ~ 1.42 THz away from the primary mode oscillate. Now, if we ignore the central-mode detuning (i.e., zero detuning), we get $p_{\text{inst}} \approx 1.078$ and $\delta\omega_{\text{inst}} \approx 1.42$ THz, which are very close to the values just mentioned. Second, we select a QCL with $\tau_{\parallel,23} = 0.036$ ps, which results in an FWHM broadening of ~ 37 meV. Reference [40] reported a similar broadening for a QCL with the bound-to-continuum design. The central-mode detuning is shown in Fig. 3.2(a) to be ~ 1.23 THz. By taking the detuning into account, we find that $p_{\text{inst}} \approx 1.04$ and $\delta\omega_{\text{inst}} \approx 1.61$ THz. However, by ignoring the central-mode detuning, we get $p_{\text{inst}} = 1$, which indicates that the laser does not have a single-mode regime—a significant error. Therefore, it is necessary to consider central-mode detuning phenomenon for broad-gain devices.

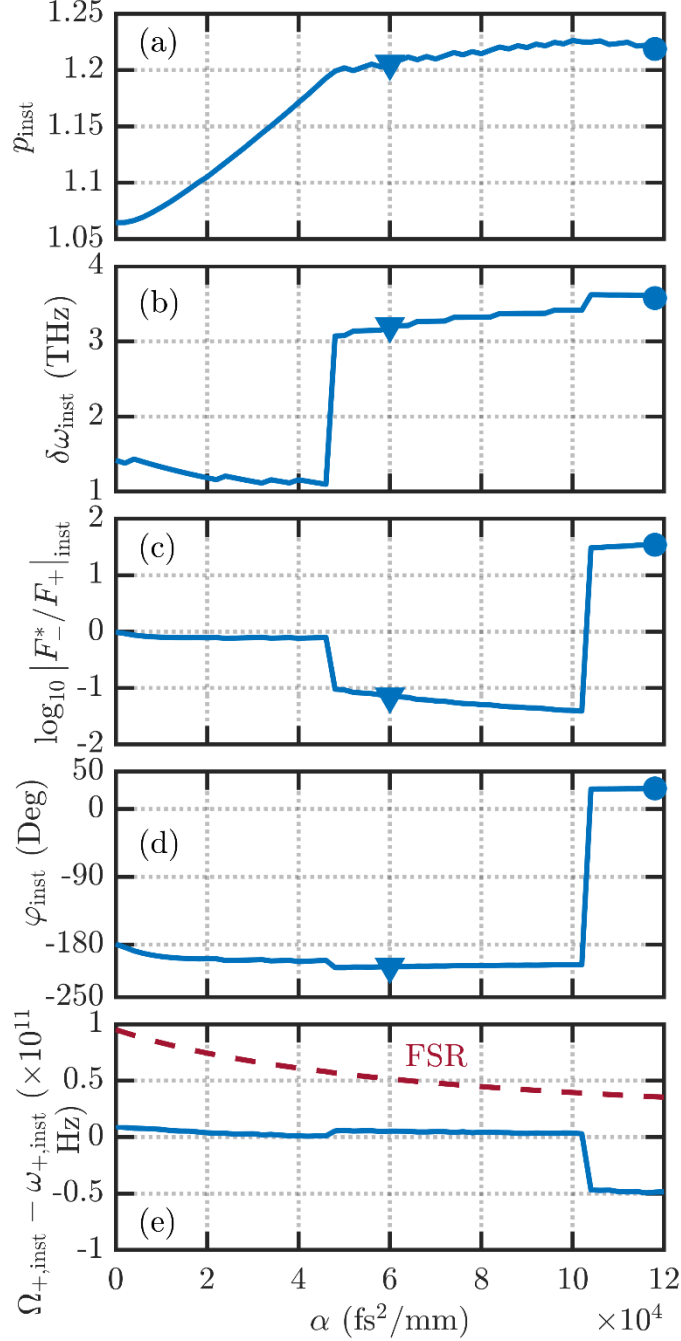


Figure 3.4: (a) Pumping level triggering the instability, (b) side-mode detuning, (c) logarithm of the amplitude ratio of the side modes, (d) relative phase φ , and (e) frequency difference between the cold- and hot-cavity modes (both corresponding to $N_{\text{side,inst}}$) as a function of positive GVD. All the quantities are taken at the instability onset. Dephasing time $\tau_{\parallel,23}$ is taken to be 0.05 ps. Solid triangle and circle are placed at points corresponding to $\alpha = 60000$ and $118000 \text{ fs}^2/\text{mm}$, respectively. The plots of $\text{Re}(g_{1,2})$, $\varphi_{1,2}$, and $\log_{10}|F_-^*/F_+|_{1,2}$ versus $\delta\omega$ for these two values of dispersion are shown in Fig. 3.5.

Now, we study the effects of the frequency-dependent refractive index on laser instability. In Fig. 3.4, we present the effects of dispersion by varying α from 0 to 120000 fs²/mm; such a wide range is chosen in order to show a complete behavior of the plotted quantities. The dephasing time of the QCL is taken as 0.05 ps [37,38]. p_{inst} and $\delta\omega_{\text{inst}}$ are plotted in Figs. 3.4(a) and 3.4(b), respectively, and the latter figure shows a jump in the side-mode detuning from ~ 1.1 to ~ 3.1 THz near $\alpha = 46000$ fs²/mm. The reason behind this sudden increase in $\delta\omega_{\text{inst}}$ will be explained shortly. In Fig. 3.4(c), we plot the logarithm of the side-mode amplitude ratio, which shows a sudden decrease near the same dispersion value where $\delta\omega_{\text{inst}}$ undergoes a jump. The ratio $|F_-^*/F_+|_{\text{inst}}$ remains close to 1 for $\alpha \leq \sim 46000$ fs²/mm. Since the relative phase is close to $-\pi$ as well, as shown in Fig. 3.4(d), the side modes show FM-like behavior for dispersion values up to ~ 46000 fs²/mm. As α goes past this value, $|F_-^*/F_+|_{\text{inst}}$ deviates significantly from 1. Specifically, the amplitude of the minus side mode is smaller than that of the plus side mode by, at least, an order of magnitude for $\sim 46000 < \alpha \leq \sim 102000$ fs²/mm. Therefore, in this dispersion range, though the relative phase remains close to $-\pi$, the side modes do not show the characteristic of an FM wave. Around $\alpha = 102000$ fs²/mm, both the amplitude ratio and the relative phase of the side modes jump. $|F_-^*/F_+|_{\text{inst}}$, again, differs considerably from 1, and now, the amplitude of the minus side mode is larger than that of the plus side mode by an order of magnitude. So, for dispersion values higher than ~ 102000 fs²/mm, though φ_{inst} is close to 0, the side modes do not demonstrate AM-like behavior.

In order to see the details, we choose two dispersion values, namely $\alpha = 60000$ and 118000 fs²/mm (points corresponding to these values are marked in Fig. 3.4), and plot the real parts of $g_{1,2}$, $\varphi_{1,2}$, and $\log_{10}|F_-^*/F_+|_{1,2}$ as a function of $\delta\omega$ (i.e., the allowed values of $\delta\omega$) in Fig. 3.5 for these values of dispersion. The graphs in Figs. 3.5(a)–3.5(c) are plotted for $\alpha = 60000$ fs²/mm and for a pumping level equal to the corresponding instability threshold. Solid triangles

are placed to denote the onset-of-instability values. Figure 3.5(a) can explain why a sudden increase in $\delta\omega_{\text{inst}}$ occurs near $46000 \text{ fs}^2/\text{mm}$ in Fig. 3.4(b). The plot of $\text{Re}(g_1)$ shows the occurrence of a local peak, referred to as “first maximum,” of negative value near 1 THz. Another local peak, “second maximum,” of positive value occurs at the solid-triangle-marked point with the corresponding frequency of ~ 3.2 THz. These frequencies are comparable to the frequencies just before and after the jump, respectively, in Fig. 3.4(b). Therefore, we deduce that, for $\alpha \leq 46000 \text{ fs}^2/\text{mm}$, the pumping required to make $\text{Re}(g_1) > 0$ in the vicinity of the first maximum is lower than the pumping required to make $\text{Re}(g_1) > 0$ in the vicinity of the second maximum. So, instability occurs near the first maximum. As α gets past $46000 \text{ fs}^2/\text{mm}$, the pumping for which $\text{Re}(g_1)$ becomes positive in the vicinity of the second maximum becomes lower. As a result, the instability point jumps from the vicinity of the first to the second maximum, causing a jump in $\delta\omega_{\text{inst}}$.

In the vicinity of the first maximum, g_1 - and g_2 -side modes behave like FM and AM waves, respectively, as shown in Figs. 3.5(b) and 3.5(c). Near the second maximum, the phases (φ_1, φ_2) are close to $(-\pi, 0)$. But, due to the significant deviation of $|F_-^*/F_+|_{1,2}$ from 1 [Fig. 3.5(c)], the modes do not show FM/AM-like behavior. Thus, Figs. 3.5(b) and 3.5(c), combined with the fact that the instability point is located near the first maximum for $\alpha \leq 46000 \text{ fs}^2/\text{mm}$ and jumps to a vicinity of the second maximum as α crosses $46000 \text{ fs}^2/\text{mm}$, explain the trends of φ_{inst} and $\log_{10} |F_-^*/F_+|_{\text{inst}}$ in Fig. 3.4 for dispersion values up to $\sim 102000 \text{ fs}^2/\text{mm}$.

The graphs in Figs. 3.5(d)–3.5(f) are plotted for $\alpha = 118000 \text{ fs}^2/\text{mm}$ and for a pumping equal to the corresponding instability threshold. The onset-of-instability points are denoted by the solid circles. As opposed to the case in Fig. 3.5(a), instability point in Fig. 3.5(d) is located on the right side of the meeting point of $\text{Re}(g_{1,2})$. In the case of a zero-GVD QCL, we have seen that

g_1 - and g_2 - modes behave as AM and FM waves, respectively, past the meeting point. However, as Fig. 3.5(f) shows, the ratios $|F_-^*/F_+|_{1,2}$ deviate from 1 by an order of magnitude, which is a significant deviation. Therefore, in this case, g_1 -side modes (g_2 -side modes) do not act as an AM (FM) wave past the meeting point of $\text{Re}(g_{1,2})$.

In Fig. 3.4(e), we plot the FSR, which is taken to be the frequency difference between the cold-cavity modes corresponding to $N_{\text{side,inst}}$ and $N_{\text{side,inst}} - 1$. The cold-cavity frequency corresponding to $N_{\text{side,inst}}$ is labeled as $\Omega_{+, \text{inst}}$ [we note that the cold-cavity mode corresponding to $N_{\text{side,inst}}$ means the mode corresponding to wavevector $(N_{23} + N_{0,\text{min}} + N_{\text{side,inst}})\pi/L$]. We also show the difference between $\Omega_{+, \text{inst}}$ and $\omega_{+, \text{inst}}$ (i.e., the hot-cavity frequency corresponding to $N_{\text{side,inst}}$). As we can see, the absolute value of this frequency difference is smaller than or comparable to the FSR in the shown dispersion range. Therefore, $\delta\omega_{\text{inst}}/\text{FSR}$ is a good approximation of $N_{\text{side,inst}}$ (i.e., the side modes that are approximately $\delta\omega_{\text{inst}}/\text{FSR}$ modes away from the primary mode oscillate when the instability sets in). The values of $\delta\omega_{\text{inst}}/\text{FSR}$ are greater than 1, indicating that the QCL undergoes harmonic instability.

Figure 3.6 shows the effects of negative dispersion on laser instability. In this case, the side-mode detuning [Fig. 3.6(a)], the amplitude ratio [Fig. 3.6(b)], and the relative phase [Fig. 3.6(c)], all show a sudden increase/decrease near $\alpha = -42000 \text{ fs}^2/\text{mm}$. For $\alpha \geq -42000 \text{ fs}^2/\text{mm}$, the side modes demonstrate FM-like behavior. As α moves toward further negative values, ϕ_{inst} jumps to a value near 0. However, $|F_-^*/F_+|_{\text{inst}}$ experiences a sudden decrease, becoming significantly smaller, i.e., an order of magnitude smaller than 1. As a result, the laser does not show AM-like behavior after being unstable. Finally, we show the frequency difference between the cold- and hot-cavity modes (both corresponding to $N_{\text{side,inst}}$) and the FSR in Fig. 3.6(d). The comparison of $\delta\omega_{\text{inst}}$ with the FSR denotes the occurrence of harmonic instability.

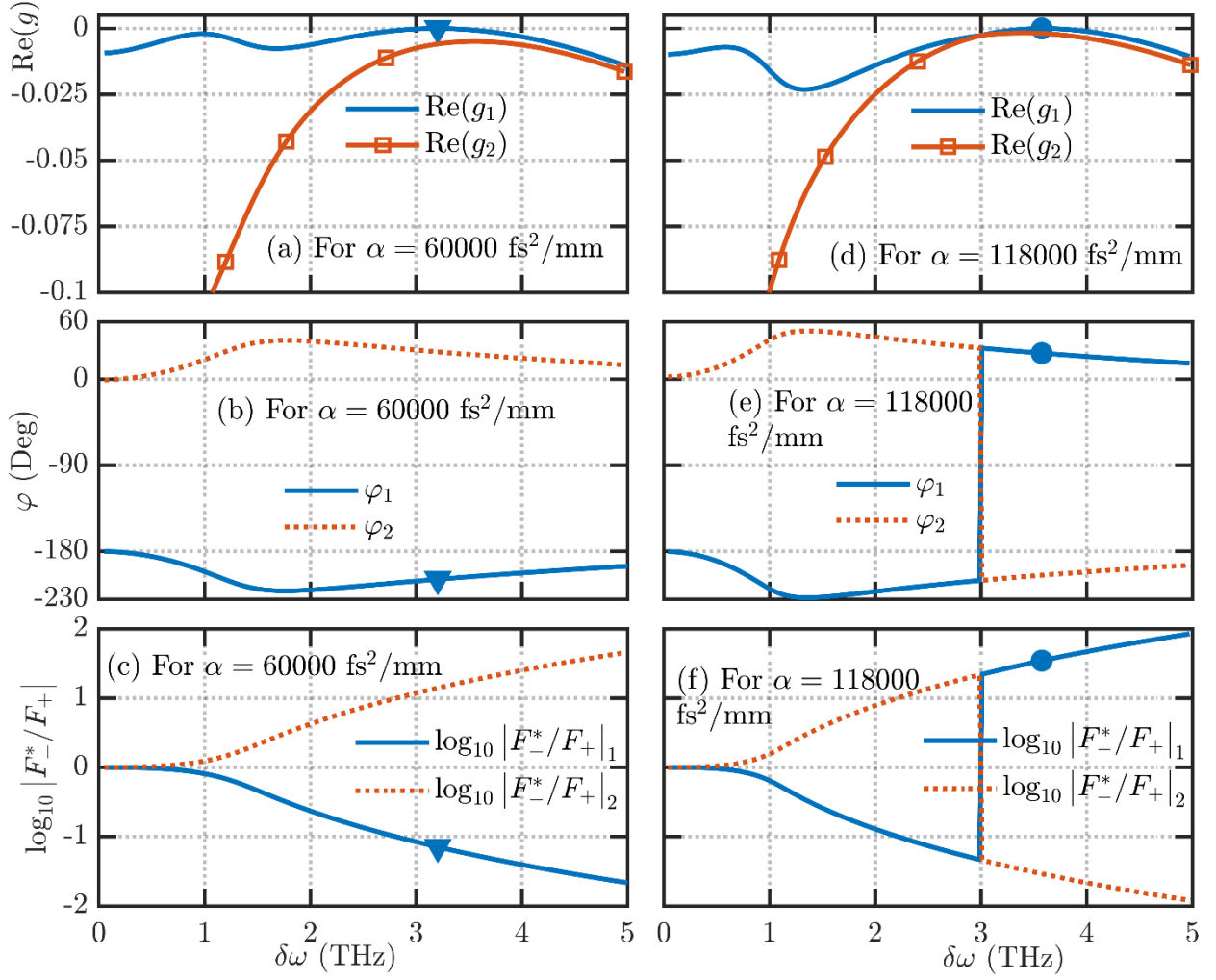


Figure 3.5: (a) and (d) Frequency dependence of real parts of $g_{1,2}$, (b) and (e) relative phases $\varphi_{1,2}$, and (c) and (f) amplitude ratios $\log_{10} |F^*/F_+|_{1,2}$ for $\alpha = 60000$ and $118000 \text{ fs}^2/\text{mm}$. The QCL has a dephasing time of 0.05 ps . For $\alpha = 60000 \text{ fs}^2/\text{mm}$ ($118000 \text{ fs}^2/\text{mm}$), the laser is pumped to a value denoted by the solid triangle (circle) in Fig. 3.4(a). Markers in this figure represent the onset-of-instability values. The detuning, the amplitude ratio, and the relative phase at these marked points are also indicated in Figs. 3.4(b)–3.4(d) with the respective markers.

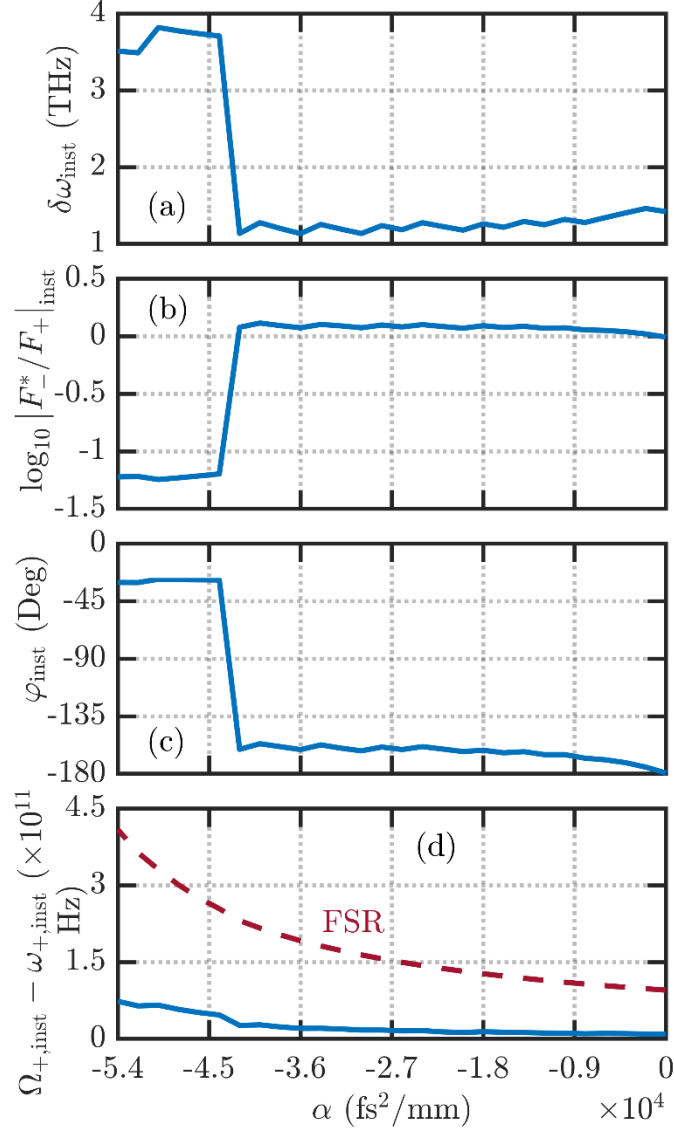


Figure 3.6: (a) side-mode detuning, (b) logarithm of the amplitude ratio of the side modes, (c) relative phase φ , and (d) frequency difference between the cold- and hot-cavity modes (both corresponding to $N_{\text{side,inst}}$) at the instability onset as a function of negative dispersion for a QCL with $\tau_{\parallel,23} = 0.05$ ps.

3.5 Summary

We have presented a detailed study of harmonic instability in an FP QCL. We have used three-level Maxwell-DM equations to derive a closed-form expression for the side-mode gain, from which all the necessary information related to instability, such as the instability threshold, the side-mode detuning at the onset of instability, and the nature of the output after the laser

becomes unstable, can be determined. Resonant tunneling, which is an important carrier-transport mechanism in QCLs, scattering rates between all three states in a period, and other laser-oscillation-related phenomena such as the detuning of the primary-mode frequency from line-center frequency and GVD have been incorporated in the model. We have shown the process to determine the central-mode detuning from the line center. Moreover, our thorough study of the effects of GVD on instability has shown that, up to a particular value of dispersion, side modes behave like an FM wave. At higher dispersion, however, they behave neither like an FM nor an AM wave.

Chapter 4: Exciting harmonic states in a quantum cascade laser via facet engineering

The content of this chapter has been submitted for journal publication and is currently under review.²

4.1 Abstract

While analyzing multimode behavior of Quantum Cascade Lasers (QCLs) using modal expansion approach, it is generally assumed that the cavity is closed, thereby completely ignoring the influence of facet reflectivity. In this chapter, we present a theory that takes into account openness of the cavity and describes the behavior of the first three modes in a QCL. Expressing spatial variations of the modes in terms of constant-flux (CF) states and exploiting biorthogonality of the CF states, we derive a set of steady-state equations for CF-state coefficients of the modes. This set of equations provides all relevant information regarding the modes. By using our theory, we show that harmonic states, i.e., states characterized by the appearance of modes that are located multiples of free spectral range away from each other, with different mode spacing can be excited by varying the length and the refractive index of a coating at a facet.

4.2 Introduction

Quantum Cascade Lasers (QCLs) are compact and powerful light sources that can operate both in the mid-infrared (mid-IR) and terahertz (THz) spectral regions. Since their inception in 1994, QCLs went through tremendous improvements both in their single mode and multimode performances. On the multimode front in particular, they were engineered to produce optical frequency combs [12,15,16]. Thus, QCLs hold great promise for applications in high-precision metrology and spectroscopy.

Investigation into the multimode regimes of QCLs was a focus of many past works [13,23,27,28,29,41]. One of the recent comprehensive studies was done by Mansuripur *et al.* [13],

² M. Roy and M. Z. Kabir, "Exciting harmonic states in a quantum cascade laser via facet engineering," *Physical Review A*, under first revision (2021).

where mode dynamics of Fabry-Perot (FP) QCLs with gradually increasing pumping level was observed. They discovered that QCLs first undergo transition from a single-mode regime into a harmonic-state regime, which is characterized by the appearance of side modes that are separated by multiples of free spectral range (FSR) from each other. With a further increase in the pumping level, the multimode character changes into the operation in a familiar conventional-state regime, marked by the appearance of single-FSR-spaced modes. In a later work, Kazakov *et al.* [12] demonstrated the frequency-comb nature of harmonic states. Besides, tuning of the mode spacing via optical seeding was achieved [42]. Although first observed in mid-IR QCLs, harmonic combs were also produced recently using THz QCLs [43,44].

Theoretical investigation into multimode behavior of QCLs can be performed in two ways: using the space-time domain simulation of the density-matrix (DM) and Maxwell's equations [37,38,45,46] or using the method of modal expansion of these equations [13,31,41,44,47]. While using the modal expansion approach, it is generally assumed that the QCL cavity is closed, i.e., the facet reflectivity is unity, and thus the mirror loss becomes zero. Therefore, the modes inside the cavity can be expressed in terms of real wavevectors and thus become power-orthogonal to each other. Although the analysis becomes simple due to the closed-cavity assumption, it completely ignores the influence of facet reflectivity on mode dynamics.

In this chapter, we present a theory that considers openness of the cavity and describes the behavior of the first three modes, i.e., a primary mode and two side modes, in a QCL. We handle the modes in the open cavity using a technique developed by Tureci *et al.* [48,49,50] In particular, spatial variations of the modes are expressed in terms of constant-flux (CF) states with an outgoing-wave boundary condition, and by exploiting biorthogonality of the CF states, we derive a set of steady-state equations (mode equations) for CF-state coefficients of the modes from the DM and Maxwell's equations. Moreover, since the three modes are locked via four-wave mixing (FWM) interaction in our formulation, the FWM locking phenomenon is included in our theory, which was not considered previously in steady-state *ab initio* laser theory (SALT) [48,49,50] and its subsequent extensions [51,52,53,54,55,56]. The mode equations derived here are valid up to a pumping level that is higher than but close to the pumping level causing primary-mode instability. Using these equations, we show that harmonic states with different mode spacing can be excited

by varying the length and the refractive index of a facet coating.

The remainder of this chapter is organized as follows. In Sec. 4.3, we derive the steady-state mode equations from the DM and Maxwell's equations. In Sec. 4.4, we apply these equations to a typical mid-IR QCL and thus show that harmonic states can be excited by varying the attributes of a facet coating. Finally, we conclude the chapter with a summary in Sec. 4.5.

4.3 Theory: From density matrix and Maxwell's equations to mode equations

We begin this section by giving an outline of our derivation of the mode equations. First, we describe carrier transport through a QCL by DM equations. We convert these equations into their frequency-domain forms and solve these via a perturbative approach, thereby finding an expression for the off-diagonal element (describes the coherence between energy levels) of the DM. Next, we assume that the laser electric field is composed of three modes, i.e., a primary mode and two side modes, and by invoking the rotating-wave approximation (RWA), we express the coherence in terms of spatial variations and frequencies of the modes. Then, we plug the expression of the coherence into Maxwell's equation and express spatial variation of each mode as a superposition of CF states. Finally, we utilize biorthogonality property of the CF states to derive steady-state equations for CF-state coefficients of the modes. These equations can be solved iteratively to find the frequencies and spatial variations of the modes.

We assume that a z -directed electric field $E(x,t)$ propagates along the x -axis of a QCL. The QCL cavity is of FP type, and, as shown in Fig. 4.1(a), the cavity employs a fully reflective coating at $x=0$. The active (gain) medium of the QCL, which consists of many heterostructure periods, starts right after $x=0$ and extends up to $x=L_1$. The linear refractive index of the active medium is n_1 , and we assume that n_1 has a positive imaginary component representing waveguide loss for the QCL. The active medium is followed by a coating of length L_2-L_1 . The coating is assumed to be optically linear to the laser field and lossy, having a complex refractive index of n_2 . The QCL is placed in a medium of refractive index n_3 . The reflectivity that the laser light encounters at $x=L_1$ depends on the length of the coating, the refractive indices of the different

media, and the light frequency. Since the cavity is closed at $x = 0$, $E(x, t) = 0$ for $x \leq 0$.

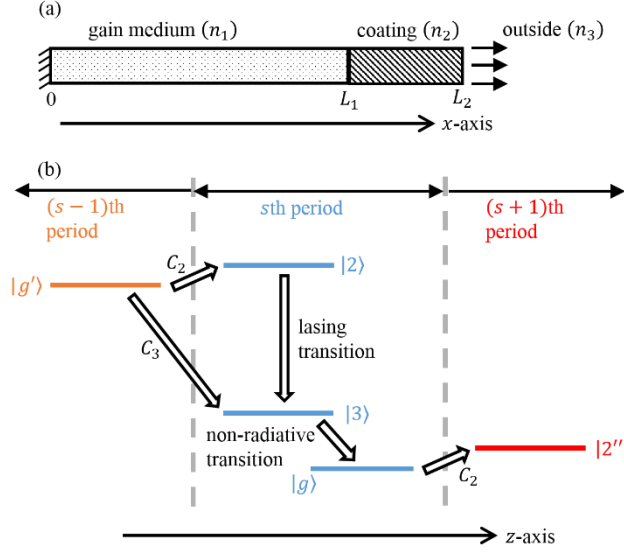


Figure 4.1: Schematic illustration of (a) the QCL cavity and (b) carrier transport through the QCL periods.

Each QCL period is assumed to have three energy levels, and carrier transport through the periods occurs in the following way [Fig. 4.1(b)]: First, electrons predominantly scatter from the ground state $|g'\rangle$ of the $(s-1)$ th period to the upper lasing state (ULS) $|2\rangle$ of the s th period by resonant tunneling; then, they mainly undergo lasing transition and reach the lower lasing state (LLS) $|3\rangle$; finally, the electrons perform non-radiative transition to the ground state $|g\rangle$ of the same period. We write the following DM equations to describe carrier transport:

$$\dot{\rho}_{22}(x, t) = C_2 - (\tau_{23}^{-1} + \tau_{2g}^{-1})\rho_{22} + iaE(x, t)(\rho_{23} - \rho_{23}^*) + D \frac{\partial^2 \rho_{22}}{\partial x^2}, \quad (4.1)$$

$$\dot{\rho}_{33}(x, t) = C_3 + \tau_{23}^{-1}\rho_{22} - \tau_{3g}^{-1}\rho_{33} + iaE(x, t)(\rho_{23}^* - \rho_{23}) + D \frac{\partial^2 \rho_{33}}{\partial x^2}, \quad (4.2)$$

$$\dot{\rho}_{23}(x, t) = -(i\omega_{23} + \tau_{\parallel}^{-1})\rho_{23} + iaE(x, t)(\rho_{22} - \rho_{33}), \quad (4.3)$$

where ρ_{22} and ρ_{33} denote normalized populations at the ULS and LLS, respectively, ρ_{23} describes the coherence between the lasing states, the overdot represents time derivative of the corresponding quantity, C_2 and C_3 are the rates of population pumping to the ULS and LLS,

respectively, τ_{ij}^{-1} is the scattering rate of carriers between the states $|i\rangle$ and $|j\rangle$, τ_{\parallel}^{-1} is the carrier dephasing rate, D represents the diffusion coefficient, and ω_{23} is the optical transition frequency ($\omega_{23} = \xi_{23}/\hbar$ with ξ_{23} denoting the energy difference between the ULS and LLS). Moreover, we define $a = ez_{23}/\hbar$, where ez_{23} represents the dipole matrix element associated with the lasing states.

Now, we take Fourier transform (FT) of the terms in Eqs. (4.1)–(4.3), thus converting the equations into their frequency-domain forms. Next, we solve these equations following a perturbative approach. To find the zero-order (with respect to the electric field) expression for population inversion, we neglect the terms containing the electric field in the population equations [frequency-domain form of Eqs. (4.1) and (4.2)], getting $\tilde{\rho}_{22}^{(0)}(\omega) - \tilde{\rho}_{33}^{(0)}(\omega) = W_{\text{eq}} 2\pi\delta(\omega)$. Here, ω is the frequency variable, $\tilde{\rho}_{ii}(x, \omega)$ is the FT of $\rho_{ii}(x, t)$, $\delta(\omega)$ is the Dirac delta function, and W_{eq} represents population inversion that would exist if the laser field was absent and is given by $W_{\text{eq}} = [C_2(\tau_{3g}^{-1} - \tau_{23}^{-1}) - C_3(\tau_{23}^{-1} + \tau_{2g}^{-1})] / [(\tau_{23}^{-1} + \tau_{2g}^{-1})\tau_{3g}^{-1}]$. Plugging this zero-order expression into the coherence equation [frequency-domain form of Eq. (4.3)] results in the first-order expression for the coherence $\tilde{\eta}^{(1)}(\omega) = iaW_{\text{eq}}H(\omega)\tilde{E}(\omega)$, where $\tilde{\eta}(x, \omega)$ and $\tilde{E}(x, \omega)$ are the FT of $\rho_{23}(x, t)$ and $E(x, t)$, respectively, and $H(\omega) = [\tau_{\parallel}^{-1} - i(\omega - \omega_{23})]^{-1}$. To find the second-order term for the population inversion $\tilde{\rho}_{22}^{(2)}(\omega) - \tilde{\rho}_{33}^{(2)}(\omega)$, we now consider terms containing the electric field in the population equations and plug into them the expression of $\tilde{\eta}^{(1)}(\omega)$. We ignore the diffusion terms for now as we do not know spatial profile of $\tilde{\rho}_{22}(x, \omega)$ and $\tilde{\rho}_{33}(x, \omega)$ yet. The sum of the zero- and second-order terms gives the full expression for the population inversion:

$$\tilde{\rho}_{22}(\omega) - \tilde{\rho}_{33}(\omega) = W_{\text{eq}} 2\pi\delta(\omega) - \frac{a^2 W_{\text{eq}}}{2\pi} Z(\omega) S(\omega), \quad (4.4)$$

$$Z(\omega) = \frac{\tau_{2g}^{-1} + \tau_{3g}^{-1} - i2\omega}{(\tau_{23}^{-1} + \tau_{2g}^{-1} - i\omega)(\tau_{3g}^{-1} - i\omega)}, \quad (4.5)$$

$$S(\omega) = \tilde{E}(\omega) \otimes [H(\omega)\tilde{E}(\omega)] + \tilde{E}^*(-\omega) \otimes [H^*(-\omega)\tilde{E}^*(-\omega)], \quad (4.6)$$

where the operator \otimes denotes the convolution operation. Finally, by inserting Eq. (4.4) into the coherence equation, we get the full expression for the coherence, which is the sum of $\tilde{\eta}^{(1)}(\omega)$ and $\tilde{\eta}^{(3)}(\omega)$:

$$\tilde{\eta}(\omega) = iaW_{\text{cq}}H(\omega)\tilde{E}(\omega) - \frac{ia^3}{4\pi^2}W_{\text{cq}}H(\omega)\left[\tilde{E}(\omega) \otimes \{Z(\omega)S(\omega)\}\right]. \quad (4.7)$$

The perturbation chain can be continued to find higher even-order and odd-order terms for the population inversion and the coherence, respectively, as done in Ref. [57]. However, the pumping levels used in this work do not significantly exceed the level triggering single-mode instability. Since the latter is close to lasing threshold for a typical FP QCL [13], inclusion of the higher-order terms is not required.

To carry our analysis forward, we now express the laser electric field in terms of a primary mode and two side modes:

$$\begin{aligned} \tilde{E}(x, \omega) = & 2\pi \sum_l A_l(x) \delta(\omega - \omega_l) \\ & + 2\pi \sum_l A_l^*(x) \delta(\omega + \omega_l), \quad l = 0, +, \text{ and } -, \end{aligned} \quad (4.8)$$

where l is a mode index, ω_0 is the frequency of the primary mode, ω_{\pm} are the side-mode frequencies, and $A_l(x)$ represents the corresponding spatial variation. Also, $\omega_{\pm} = \omega_0 \pm \Delta\omega$, where $\Delta\omega$ is the frequency detuning of the side modes from the primary mode. The side modes have been assumed to be detuned equally from the primary mode because of the FWM locking phenomenon. The equality in the side-mode spacing was observed in the experiment as well [12]. The spatial variations and the frequencies are considered to be unknown. Next, to get an expression of the coherence in terms of $A_l(x)$ and ω_l , we insert Eq. (4.8) into Eq. (4.7) and invoke the RWA. After simplification, we get

$$\begin{aligned}
\tilde{\eta}(\omega) = & iaW_{\text{eq}} 2\pi \sum_{l=0,+,-} \left[A_l H(\omega_l) \delta(\omega - \omega_l) \right] \\
& - ia^3 W_{\text{eq}} 2\pi \left[H(\omega_0) \{ Z(0) B_{\text{dc}} A_0 + Z(\Delta\omega) B_{\Delta} A_- + Z^*(\Delta\omega) B_{\Delta}^* A_+ \} \delta(\omega - \omega_0) \right. \\
& + H(\omega_+) \{ Z(0) B_{\text{dc}} A_+ + Z(\Delta\omega) B_{\Delta} A_0 + Z(2\Delta\omega) B_{2\Delta} A_- \} \delta(\omega - \omega_+) \\
& \left. + H(\omega_-) \{ Z(0) B_{\text{dc}} A_- + Z^*(\Delta\omega) B_{\Delta}^* A_0 + Z^*(2\Delta\omega) B_{2\Delta}^* A_+ \} \delta(\omega - \omega_-) \right],
\end{aligned} \tag{4.9}$$

$$B_{\text{dc}} = \sum_{l=0,+,-} A_l A_l^* [H(\omega_l) + H^*(\omega_l)], \tag{4.10}$$

$$B_{\Delta} = A_+ A_0^* [H(\omega_+) + H^*(\omega_0)] + A_0 A_-^* [H(\omega_0) + H^*(\omega_-)], \tag{4.11}$$

$$B_{2\Delta} = A_+ A_-^* [H(\omega_+) + H^*(\omega_-)]. \tag{4.12}$$

To understand how the subscripts to B have been chosen, we need to look at the expression of $S(\omega)$:

$$S(\omega) = (2\pi)^2 \left[B_{\text{dc}} \delta(\omega) + B_{\Delta} \delta(\omega - \Delta\omega) + B_{2\Delta} \delta(\omega - 2\Delta\omega) + B_{\Delta}^* \delta(\omega + \Delta\omega) + B_{2\Delta}^* \delta(\omega + 2\Delta\omega) \right]. \tag{4.13}$$

As it shows, the B terms are the coefficients of the delta functions, and their subscripts have been chosen to correspond to the frequencies of the associated delta functions. Since the electric field consists of three frequencies, the term $S(\omega)$, and thus the population inversion, oscillates at $\Delta\omega$ and $2\Delta\omega$ difference frequencies.

Having found the coherence, we now calculate its impact on the laser field by using Maxwell's wave equation:

$$\frac{\partial^2}{\partial x^2} E(x, t) - \frac{1}{c^2} \frac{\partial^2}{\partial t^2} E(x, t) = \frac{1}{\epsilon_0 c^2} \frac{\partial^2}{\partial t^2} \left[P_{\text{back}}(x, t) + P_{\text{three-level}}(x, t) \right]. \tag{4.14}$$

Here, c is the speed of light in free space and ϵ_0 is the vacuum permittivity. P_{back} , the nonresonant component of the total polarization, represents the linear polarization of the background host material in the active and coating regions. $P_{\text{three-level}}$, the resonant component of the total polarization, represents the polarization due to the three-level QCL periods (zero inside the coating). Allowing for the possibility of the material in the active region to be dispersive, we write

the nonresonant part of the polarization as $P_{\text{back}}(x, t) = \varepsilon_0 \chi_{\text{back}}(x, t) \otimes E(x, t)$, where $\chi_{\text{back}}(x, t)$ is the corresponding electric susceptibility; the time-dependent nature of the susceptibility is due to dispersion. The resonant part can be written as $P_{\text{three-level}} = -N(x) \Gamma a \hbar (\rho_{23} + \rho_{23}^*)$, where $N(x)$ is the concentration of free electrons (assumed uniform in the active region and zero in the coating region) and Γ represents the overlap factor between the optical field and the active region. Now, converting Eq. (4.14) into its frequency-domain form and considering only the positive frequencies, we get

$$\frac{\partial^2}{\partial x^2} \tilde{E}(x, \omega) + \frac{n^2(x, \omega) \omega^2}{c^2} \tilde{E}(x, \omega) = \frac{N(x) \Gamma a \hbar \omega^2}{\varepsilon_0 c^2} \tilde{\eta}(x, \omega). \quad (4.15)$$

Here, we have introduced a space- and frequency-dependent refractive index through $n^2(x, \omega) = 1 + \tilde{\chi}_{\text{back}}(x, \omega)$, where $\tilde{\chi}_{\text{back}}(x, \omega)$ is the FT of $\chi_{\text{back}}(x, t)$. For the cavity shown in Fig. 4.1(a), $n(x, \omega) = n_1(\omega)$ for $0 < x \leq L_1$, $n(x, \omega) = n_2$ for $L_1 < x \leq L_2$, and $n(x, \omega) = n_3$ otherwise. Next, we plug Eqs. (4.8) and (4.9) into Eq. (4.15) and equate the terms with the same delta function, and it results in the following equations for the spatial variations $A_l(x)$:

$$\begin{aligned} \frac{\partial^2}{\partial x^2} A_0 + \frac{n^2(x, \omega_0) \omega_0^2}{c^2} A_0 &= \frac{iN(x) \Gamma a^2 \hbar \omega_0^2 W_{\text{eq}} H(\omega_0)}{\varepsilon_0 c^2} \\ &\times \left[A_0 - a^2 \left\{ Z(0) B_{\text{dc}} A_0 + Z(\Delta\omega) B_{\Delta} A_- + Z^*(\Delta\omega) B_{\Delta}^* A_+ \right\} \right], \end{aligned} \quad (4.16)$$

$$\begin{aligned} \frac{\partial^2}{\partial x^2} A_+ + \frac{n^2(x, \omega_+) \omega_+^2}{c^2} A_+ &= \frac{iN(x) \Gamma a^2 \hbar \omega_+^2 W_{\text{eq}} H(\omega_+)}{\varepsilon_0 c^2} \\ &\times \left[A_+ - a^2 \left\{ Z(0) B_{\text{dc}} A_+ + Z(\Delta\omega) B_{\Delta} A_0 + Z(2\Delta\omega) B_{2\Delta} A_- \right\} \right], \end{aligned} \quad (4.17)$$

$$\begin{aligned} \frac{\partial^2}{\partial x^2} A_- + \frac{n^2(x, \omega_-) \omega_-^2}{c^2} A_- &= \frac{iN(x) \Gamma a^2 \hbar \omega_-^2 W_{\text{eq}} H(\omega_-)}{\varepsilon_0 c^2} \\ &\times \left[A_- - a^2 \left\{ Z(0) B_{\text{dc}} A_- + Z^*(\Delta\omega) B_{\Delta}^* A_0 + Z^*(2\Delta\omega) B_{2\Delta}^* A_+ \right\} \right]. \end{aligned} \quad (4.18)$$

These equations hold for all x : For $x > L_1$, $A_l(x)$ are nonzero above lasing threshold but the right-

hand sides of the equations vanish.

In most of the previous works that used modal expansion approach to analyze multimode characteristics of QCLs, the laser cavity was assumed to be closed, and hence, spatial variation of a mode was expressed in terms of a real wavevector [13,31,41,44,47]. This approach is not applicable in our case as we are dealing with an open cavity. So, we follow the technique developed by Tureci and coauthors [48,49,50] and express the spatial variations in terms of CF states with an outgoing-wave boundary condition. We represent these CF states as $\psi_m(x, \omega_l) \equiv \psi_{ml}(x)$; since an infinite number of CF states exists for a value of ω_l , we have used m , an integer, that serves as an index to the CF state. Let us take $k_l = \omega_l/c$, where k_l (real) represents the wavevector of the laser field in free space. Then, for the cavity in Fig. 4.1(a), ψ_{ml} satisfies the following equations:

$$\psi_{ml} = 0, \quad x \leq 0, \quad (4.19)$$

$$\frac{\partial^2}{\partial x^2} \psi_{ml} = -n_{1l}^2 \kappa_{ml}^2 \psi_{ml}, \quad 0 < x \leq L_1, \quad (4.20)$$

$$\frac{\partial^2}{\partial x^2} \psi_{ml} = -n_2^2 k_l^2 \psi_{ml}, \quad L_1 < x \leq L_2, \quad (4.21)$$

$$\psi_{ml} = F_{ml} e^{in_3 k_l (x - L_2)}, \quad x > L_2. \quad (4.22)$$

Here, $n_{1l} \equiv n_1(k_l c)$, $\kappa_{ml} \equiv \kappa_m(k_l)$ is the wavevector of ψ_{ml} inside the active region (CF wavevector) and complex, and F_{ml} is the amplitude of the outgoing exponential function. In addition, ψ_{ml} has to satisfy the continuity conditions at the interfaces [48]. By combining Eqs. (4.19) and (4.20), CF states in the active region can be written as

$$\psi_{ml}(x) = \sin(n_{1l} \kappa_{ml} x), \quad 0 < x \leq L_1. \quad (4.23)$$

Next, we use the continuity conditions to smoothly connect different parts of ψ_{ml} at the interfaces. Thus, we get the following equation that produces all the allowed CF wavevectors κ_{ml} for a given value of k_l :

$$\tan(n_{1l} \kappa_{ml} L_1) = \frac{n_{1l} \kappa_{ml}}{ik_l} \frac{1}{n_2} \frac{i n_3 \sin[n_2 k_l (L_2 - L_1)] - n_2 \cos[n_2 k_l (L_2 - L_1)]}{i n_2 \sin[n_2 k_l (L_2 - L_1)] - n_3 \cos[n_2 k_l (L_2 - L_1)]}. \quad (4.24)$$

CF states are not power-orthogonal, but they are biorthogonal to their adjoint states $\phi_{ml}(x) = \psi_{ml}^*(x)$; that means,

$$n_{1l}^2 \int_0^{L_1} \psi_{ml} \phi_{r'l}^* dx = \delta_{mr} \sigma_{ml}. \quad (4.25)$$

Here, δ_{mr} is the Kronecker delta and $\sigma_{ml} \equiv \sigma_m(k_l)$ is a normalization parameter. The integration has been taken to be performed over the active region only [58]. By putting Eq. (4.23) into Eq. (4.25), we get the normalization parameter to be $\sigma_{ml} = (n_{1l}^2 L_1 / 2) [1 - \sin(2n_{1l} \kappa_{ml} L_1) / (2n_{1l} \kappa_{ml} L_1)]$.

We now express $A_l(x)$ in the active region as a superposition of the CF states:

$$A_l(x) = \sum_m b_{ml} \psi_{ml} = \sum_m b_{ml} \sin(n_{1l} \kappa_{ml} x), \quad 0 < x \leq L_1, \quad (4.26)$$

where b_{ml} are the corresponding CF-state coefficients. To get steady-state equations for these coefficients, we put Eq. (4.26) into differential Eqs. (4.16)–(4.18), multiply the equations by $\phi_{r'l}^*$, and exploit biorthogonality of the CF states. After simplification, we get

$$\begin{aligned} & -b_{rl} - ip W_{\text{th}}' \frac{k_l^2}{\kappa_{rl}^2 - k_l^2} \frac{1}{1 - ic\tau_{\parallel}(k_l - k_{23})} \frac{1}{n_{1l}^2} \\ & \times \left[b_{rl} - \frac{a^2 n_{1l}^2}{\sigma_{rl}} \int_0^{L_1} G_l(x) \sin(n_{1l} \kappa_{rl} x) dx \right] = 0, \quad l = 0, +, \text{ and } -, \quad r \in \{\text{integers}\}, \end{aligned} \quad (4.27)$$

$$G_0(x) = Z(0) B_{\text{dc}} A_0 + Z(\Delta k) B_{\Delta} A_- + Z^*(\Delta k) B_{\Delta}^* A_+, \quad (4.28)$$

$$G_+(x) = Z(0) B_{\text{dc}} A_+ + Z(\Delta k) B_{\Delta} A_0 + Z(2\Delta k) B_{2\Delta} A_-, \quad (4.29)$$

$$G_-(x) = Z(0) B_{\text{dc}} A_- + Z^*(\Delta k) B_{\Delta}^* A_0 + Z^*(2\Delta k) B_{2\Delta}^* A_+, \quad (4.30)$$

where p is the pumping parameter and is given by $p = W_{\text{eq}} / W_{\text{th}}$, W_{th} is the threshold population inversion, $W_{\text{th}}' = N\Gamma a^2 \hbar \tau_{\parallel} W_{\text{th}} / \varepsilon_0$ represents the scaled threshold inversion (dimensionless), $k_{23} = \omega_{23} / c$, $\Delta k = \Delta\omega / c$, and $Z(\Delta k) \equiv Z(c\Delta k)$. If we set B_{Δ} and $B_{2\Delta}$ to zero, thereby ignoring the

oscillation of population inversion, Eq. (4.27) will essentially be reduced to a third-order version of the SALT equation (Eq. (7) in Ref. [49]).

Now that we know the functional form of $A_l(x)$, we can include the diffusion coefficient D in our analysis. By inserting Eq. (4.26) \rightarrow Eq. (4.13) \rightarrow Eq. (4.4), we see that the second-order population terms $\tilde{\rho}_{22}^{(2)}$ and $\tilde{\rho}_{33}^{(2)}$ take the form $\tilde{\rho}_{ii}^{(2)}(x, \omega) \sim \sum_{m,l,m',l'} \cos(n_{1l} \kappa_{ml} x \mp n_{1l'}^* \kappa_{m'l'}^* x)$. Then, from the frequency-domain form of Eqs. (4.1) and (4.2), one can deduce that the diffusion phenomenon can be included by replacing $\tau_{2g}^{-1} \rightarrow \tau_{2g}^{-1} + D(n_{1l} \kappa_{ml} \mp n_{1l'}^* \kappa_{m'l'}^*)^2$ and $\tau_{3g}^{-1} \rightarrow \tau_{3g}^{-1} + D(n_{1l} \kappa_{ml} \mp n_{1l'}^* \kappa_{m'l'}^*)^2$ in $Z(\omega)$. Since $Z(\omega)$ no longer remains independent of the CF wavevectors, the products of Z and B cannot be written as those in Eqs. (4.28)–(4.30). Let us consider that the mode indices 0, +, and – correspond to the integers 0, 1, and –1, respectively. Then, by inserting Eq. (4.26) into Eqs. (4.28)–(4.30), we find that $G_l(x)$ can be expressed as a sum of terms of the following form:

$$\begin{aligned}
U_{l',l'',l-l'+l''}(x) &= \frac{1}{2} [H(k_{l'}) + H^*(k_{l''})] \sum_{m',m'',m'''} [b_{m'l'} b_{m''l''}^* b_{m'''(l-l'+l'')} \\
&\times \{ Z_{m',l',m'',l''}^- \cos(n_{1l'} \kappa_{m'l'} x - n_{1l''}^* \kappa_{m''l''}^* x) - Z_{m',l',m'',l''}^+ \cos(n_{1l'} \kappa_{m'l'} x + n_{1l''}^* \kappa_{m''l''}^* x) \} \\
&\times \sin(n_{1(l-l'+l'')} \kappa_{m'''(l-l'+l'')} x) \Big]. \quad (4.31)
\end{aligned}$$

Here, m' , m'' , and m''' are CF-state indices corresponding to the mode indices l' , l'' , and $l-l'+l''$, respectively. Also, $H(k_{l'}) \equiv H(ck_{l'})$ and

$$\begin{aligned}
Z_{m',l',m'',l''}^\mp &= \frac{\tau_{2g}^{-1} + \tau_{3g}^{-1} + 2D(n_{1l'} \kappa_{m'l'} \mp n_{1l''}^* \kappa_{m''l''}^*)^2 - i2c\Delta k(l' - l'')}{\tau_{23}^{-1} + \tau_{2g}^{-1} + D(n_{1l'} \kappa_{m'l'} \mp n_{1l''}^* \kappa_{m''l''}^*)^2 - ic\Delta k(l' - l'')} \\
&\times \frac{1}{\tau_{3g}^{-1} + D(n_{1l'} \kappa_{m'l'} \mp n_{1l''}^* \kappa_{m''l''}^*)^2 - ic\Delta k(l' - l'')} . \quad (4.32)
\end{aligned}$$

Equation (4.31) can be visualized in terms of the correspondence $U_{l',l'',l-l'+l''} \leftrightarrow A_{l'} A_{l''}^* A_{l-l'+l''}$; they would be proportional to each other in the absence of carrier diffusion. Finally, $G_l(x)$ becomes

$$G_l(x) = \sum_{\substack{l',l'' \\ -1 \leq l-l'+l'' \leq 1}} U_{l',l'',l-l'+l''}(x). \quad (4.33)$$

Equation (4.27), with $G_l(x)$ given by Eq. (4.33), represents the set of final mode equations, which can be used to find the CF-state coefficients b_{rl} and the wavevectors k_l .

4.4 Results and discussion

For simulations, we choose a typical mid-IR QCL with a short gain recovery time. Its parameters are given in Table 4.1. We consider the waveguide loss by taking the refractive index of the active medium n_1 to be complex with the imaginary part given by $\text{Im}(n_1) = (c \times \text{amplitude of waveguide loss})/\omega_{23}$. Also, we take the active medium to be nondispersive in our simulation.

Table 4.1: Parameters of the mid-IR QCL used for simulations in this chapter [20,38]

Parameters	Values	Parameters	Values
Uls \rightarrow LLS scattering rate, τ_{23}^{-1}	$(1 \text{ ps})^{-1}$	Amplitude waveguide loss	10 cm^{-1}
Uls $\rightarrow g\rangle$ scattering rate, τ_{2g}^{-1}	$(3 \text{ ps})^{-1}$	Refractive index of the active medium, n_1	$3.3 + 0.00099i$
LLS $\rightarrow g\rangle$ scattering rate, τ_{3g}^{-1}	$(0.1 \text{ ps})^{-1}$	Dipole matrix element, z_{23}	2 nm
Carrier dephasing rate, $\tau_{ }^{-1}$	$(0.08 \text{ ps})^{-1}$	Length of the active region, L_1	3 mm
Free-space wavelength corresponding to the line-center wavevector k_{23}	$6.2 \text{ }\mu\text{m}$	Diffusion coefficient, D	$77 \text{ cm}^2/\text{s}$

First, let us discuss lasing threshold. To determine the scaled threshold inversion and the

wavevector of the primary mode at threshold, we ignore the nonlinear part in Eq. (4.27) and set the mode index $l = 0$. Equating the imaginary part of the equation to zero gives

$$k_0^2 \operatorname{Re} \left[\frac{1}{\kappa_{00}^2 - k_0^2} \frac{1}{1 - ic\tau_{\parallel} (k_0 - k_{23})} \frac{1}{n_1^2} \right] = 0, \quad (4.34)$$

where $n_{1l=0} \equiv n_1$ because there is no dispersion. Equation (4.34) and the CF eigenvalue equation (4.24) need to be solved simultaneously to find k_0 and κ_{00} . Equation (4.24) produces an infinite number of κ_{r0} for a value of k_0 , and the difference between the real parts of κ_{r0} and $\kappa_{(r+1)0}$ is close to the FSR of the laser $\pi / [\operatorname{Re}(n_1)L_1]$. However, Eq. (4.34) is satisfied by certain discrete values of k_0 and only one CF wavevector $\kappa_{(r=0)0}$ for each of these discrete values. The spacing between the two consecutive values of k_0 is typically close to the FSR. Now, inserting the values of k_0 and κ_{00} into the following equation, which is obtained by equating the real part of Eq. (4.27) to zero, we get the corresponding scaled threshold inversion:

$$W_{\text{th}}' = \left\{ k_0^2 \operatorname{Im} \left[\frac{1}{\kappa_{00}^2 - k_0^2} \frac{1}{1 - ic\tau_{\parallel} (k_0 - k_{23})} \frac{1}{n_1^2} \right] \right\}^{-1}. \quad (4.35)$$

In Fig. 4.2, we plot W_{th}' as a function of $k_0 - k_{23}$ (normalized by the FSR) for the two facet settings: First, the facet is uncoated ($L_2 - L_1 = 0$), and second, a coating of length $L_2 - L_1 = 0.14$ mm with $n_2 = 1.55 + 0.00099i$ is applied to the facet. The values in the second case are chosen to explain the way of exciting harmonic states, as we will see later. In both cases, we assume the environment surrounding the laser to be free space. Also, the line-center wavevector k_{23} is chosen to be close to one of the values of k_0 that satisfy Eq. (4.34). As Fig. 4.2 shows, there exists a global minimum for each curve, and the primary mode is expected to start lasing at the wavevector corresponding to the minimum point of the curve [23]. We denote the values of k_0 , κ_{00} , and W_{th}' at the minimum point as \bar{k}_{th} , $\bar{\kappa}_{\text{th}}$, and \bar{W}_{th}' , respectively. Moreover, Fig. 4.2 shows that the reflection coefficient of a facet can have strong influence on the shape of the scaled threshold function. For the uncoated case, the reflection coefficient (~ 0.286) is independent of the wavelength of the laser, and so,

W_{th}' takes the form of the reciprocal of the Lorentzian gain function. However, for the coated case, the facet reflectivity depends on the wavelength, which, in turn, causes the mirror loss to modulate with the wavelength. As a result, multiple minima appear in W_{th}' , as depicted in Fig. 4.2.

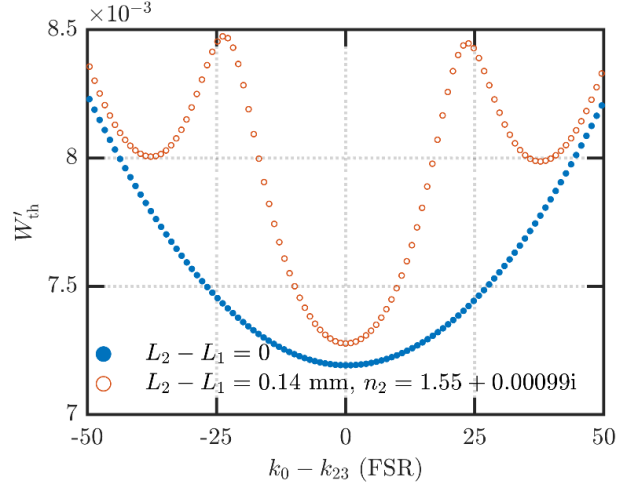


Figure 4.2: Scaled threshold function for the uncoated and coated facet. In both cases, the cavity is assumed to be placed in free space.

We now focus on the single-mode regime. We suppose that the primary mode is composed of three CF states with wavevectors κ_{00} and $\kappa_{\pm 10}$; κ_{00} is close to $\bar{\kappa}_{\text{th}}$, κ_{-10} is the wavevector adjacent to κ_{00} with $\text{Re}(\kappa_{-10}) < \text{Re}(\kappa_{00})$, and κ_{10} is adjacent to κ_{00} with $\text{Re}(\kappa_{10}) > \text{Re}(\kappa_{00})$. Since the coefficients $b_{r,0}$ are nonzero above lasing threshold, we must take the nonlinear part in Eq. (4.27) into consideration. Thus, the primary-mode equation becomes

$$\begin{aligned}
 & -b_{r,0} - i p \bar{W}'_{\text{th}} \frac{k_0^2}{\kappa_{r,0}^2 - k_0^2} \frac{1}{1 - i c \tau_{\parallel} (k_0 - k_{23})} \frac{1}{n_1^2} \\
 & \times \left[b_{r,0} - \frac{a^2 n_1^2}{\sigma_{r,0}} \int_0^{L_1} U_{0,0,0}(x) \sin(n_1 \kappa_{r,0} x) dx \right] = 0.
 \end{aligned} \tag{4.36}$$

The unknowns $b_{r,0}$, k_0 , and $\kappa_{r,0}$ can be found by solving Eqs. (4.36) and (4.24) iteratively. Since Eq. (4.36) is invariant under the transformation $\{b_{r,0}\} \rightarrow e^{i\theta_0} \{b_{r,0}\}$ for an arbitrary phase angle θ_0 , it is necessary to keep the phase angle of any one of $b_{r,0}$ constant throughout the solving process.

This is known as the “gauge fixing requirement (GFR)” [49]. Following Ge [58], we implement the GFR by tuning the value of the lasing wavevector k_0 so that the dominant b_{r_0} , i.e., b_{00} , becomes a real quantity and remains so throughout the iterations. This procedure allows us to obtain k_0 above threshold. (We have repeated the procedure with the other b_{r_0} instead of b_{00} and have obtained similar solutions for k_0) In Fig. 4.3, we show the ratio $\log_{10}|b_{00}/b_{-10}|$ as a function of the pumping parameter for $n_3 = 1$ and 2.7. The coating length is set to zero. A refractive index of 2.7 for n_3 results in a frequency-independent facet reflectivity of 0.01. Note that, in Fig. 4.3, we have disregarded lasing of the $+/-$ side modes although the primary-mode instability has occurred at a pumping level much lower than 1.15. The coefficients b_{10} and b_{-10} are similar in values, so we choose only one of them for plotting. According to Fig. 4.3, even though the ratio $|b_{00}/b_{-10}|$ decreases with increasing pumping level and with increasing openness of the cavity, b_{00} remains at least an order of magnitude larger than b_{-10} . Therefore, in the following simulations, we will represent spatial variation of a mode in terms of a single CF state. Moreover, the detuning of k_0 from its value at threshold, \bar{k}_{th} , is found to be small (not shown).

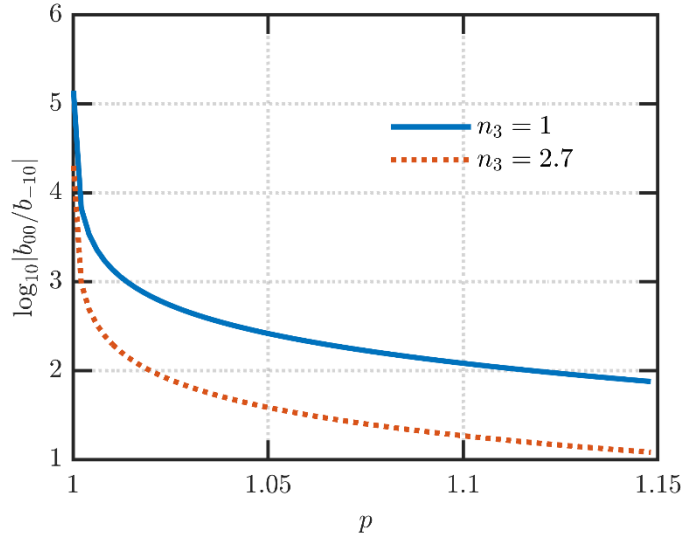


Figure 4.3: Ratio of the CF-state coefficients corresponding to the primary mode for $n_3 = 1$ and 2.7. The coating length is set to zero.

Having solved the mode equation for the primary mode, we now investigate its stability. For linear stability, we can drop the terms in Eq. (4.27) that are of second and third order in $b_{r(l=+,-)}$. Then, the primary-mode equation decouples from the side-mode equations and reduces to Eq. (4.36). For the side modes, we can set up the following eigenvalue equations:

$$\begin{aligned}
& -b_{r+} - ip\bar{W}'_{\text{th}} \frac{k_+^2}{\kappa_{r+}^2 - k_+^2} \frac{1}{1 - ic\tau_{\parallel}(k_+ - k_{23})} \frac{1}{n_1^2} \\
& \times \left[b_{r+} - \frac{a^2 n_1^2}{\sigma_{r+}} \int_0^{L_1} \left(U_{0,0,+} + \underbrace{U_{+,0,0} + U_{0,-,0}}_{\text{population oscillation}} \right) \sin(n_1 \kappa_{r+} x) dx \right] = \gamma b_{r+},
\end{aligned} \tag{4.37}$$

$$\begin{aligned}
& -b_{s-}^* + ip\bar{W}'_{\text{th}} \frac{k_-^2}{\kappa_{s-}^{*2} - k_-^2} \frac{1}{1 + ic\tau_{\parallel}(k_- - k_{23})} \frac{1}{n_1^2} \\
& \times \left[b_{s-}^* - \frac{a^2 n_1^{*2}}{\sigma_{s-}^*} \int_0^{L_1} \left(U_{0,0,-}^* + \underbrace{U_{0,+,-}^* + U_{-,0,0}^*}_{\text{population oscillation}} \right) \sin(n_1^* \kappa_{s-}^* x) dx \right] = \gamma b_{s-}^*,
\end{aligned} \tag{4.38}$$

where s is a CF-state index. Equations (4.37) and (4.38) can be represented in the form $[B][b_{r+} \ b_{s-}^*]^T = \gamma [b_{r+} \ b_{s-}^*]^T$, where γ is the eigenvalue (dimensionless) of the coefficient matrix $[B]$ and the superscript T stands for the transpose operation. For the primary mode to become unstable, one of the values of γ needs to satisfy the following two conditions:

$$\text{Im}(\gamma) = 0 \quad \text{and} \quad \text{Re}(\gamma) > 0. \tag{4.39}$$

We denote the pumping level for which Eq. (4.39) is satisfied as p_i . The nature of the side modes, i.e., whether they behave like a frequency-modulated (FM) or an amplitude-modulated (AM) wave, can be understood from the relative phase $\Theta = \arg(F_-^*) - \arg(F_+) - 2\arg(F_0)$ and the side-mode amplitude ratio $|F_-/F_+|$. Here, F_l represents the total amplitude of the outgoing exponential function for mode l . In particular, $F_l = \sum_r F_{rl} b_{rl}$, where F_{rl} is the amplitude of the outgoing exponential function as defined in Eq. (4.22).

Now, we take each of the three modes to be composed of a single CF state. Denoting the CF-state coefficients and CF wavevectors corresponding to the side modes as $b_{0\pm}$ and $\kappa_{0\pm}$,

respectively, we calculate the eigenvalue γ using Eqs. (4.37) and (4.38). Of the two values of γ at each Δk , we are only interested in the value whose real part is larger. Figure 4.4(a) shows $\text{Re}(\gamma)$ as a function of the side-mode detuning Δk (normalized by the FSR) for the following three facet settings: $L_2 - L_1 = 0$ with $n_3 = 1$, $L_2 - L_1 = 0$ with $n_3 = 2.7$, and $L_2 - L_1 = 0.14$ mm with $n_2 = 1.55 + 0.00099i$ and $n_3 = 1$. Only those values of γ that satisfy the first condition in Eq. (4.39) are chosen for plotting. Also, pumping level is set to respective p_i . As indicated by the arrow, $\text{Re}(\gamma)$ becomes positive, and thus instability occurs, at a detuning of ~ 1 FSR in all three cases. Moreover, the eigenvalue is zero at zero detuning, which can be explained in the following way. At zero detuning, only the terms that represent population oscillation survive in Eqs. (4.37) and (4.38). The other terms add up to zero since the primary mode is lasing. Now, recalling the correspondence $U_{l',l'',l-l'+l''} \leftrightarrow A_{l'} A_{l''}^* A_{l-l'+l''}$, and then by pulling out b_{0+} and b_{0-}^* from U , one can deduce that the determinant of B should be zero. Hence, γ should be zero as well. Figure 4.4(b) shows the pumping level p_i for $n_3 = 1, 1.5, 2,$ and 2.7 with the coating length being set to zero. As the facet reflectivity decreases, the primary mode becomes unstable at a lower pumping level. In Fig. 4.4(c), we plot Θ and the side-mode amplitude ratio (both at the onset of instability) for the same values of n_3 . In all the cases, the side modes are found to behave like an FM wave.

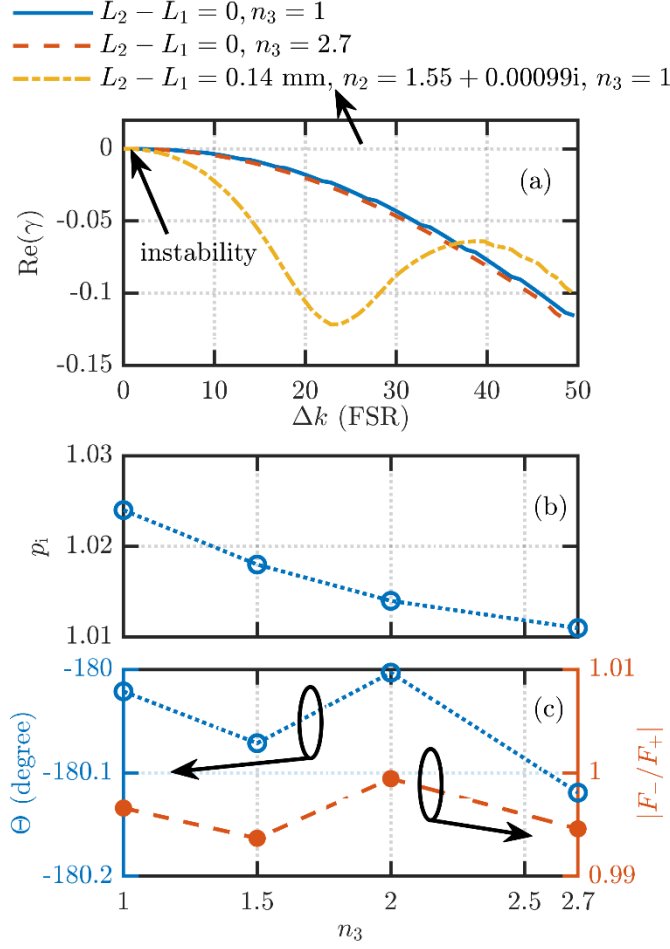


Figure 4.4: (a) Real part of the eigenvalue γ at the onset of instability for three different facet settings. (b) Pumping level triggering single-mode instability for $n_3 = 1, 1.5, 2,$ and 2.7 . (c) The relative phase Θ and the side-mode amplitude ratio at the onset of instability for the same four values of n_3 . The coating length is zero for (b) and (c).

The coefficient matrix $[B]$ can be written as a sum of two matrices $[B]_{\text{L}}$ and $[B]_{\text{NL}}$, where $[B]_{\text{L}}$ represents the linear contribution (diagonal matrix) and $[B]_{\text{NL}}$ represents the nonlinear contribution (due to U). Then, assuming that the eigenvector $[b_{0+} \ b_{0-}^*]^T$ is normalized, we can split the eigenvalue γ into linear and nonlinear parts where the linear part $\gamma_{\text{L}} = [b_{0+} \ b_{0-}^*]^* [B]_{\text{L}} [b_{0+} \ b_{0-}^*]^T$ and the nonlinear part $\gamma_{\text{NL}} = [b_{0+} \ b_{0-}^*]^* [B]_{\text{NL}} [b_{0+} \ b_{0-}^*]^T$. In Fig. 4.5, we show the breakdown of $\text{Re}(\gamma)$ into their respective linear and nonlinear parts for the

same facet settings as those in Fig. 4.4(a). The second maximum of $\text{Re}(\gamma_L)$ in Fig. 4.5(c) corresponds to the two local minima (on each side of the global minimum) of W_{th}' in Fig. 4.2 (orange curve). Figure 4.5 shows that, in the vicinity of zero detuning, $\text{Re}(\gamma_L)$ is a decreasing function whereas $\text{Re}(\gamma_{\text{NL}})$ is a slowly increasing function. Also, the sum of these two functions is zero at zero detuning. Therefore, instability occurs at a point adjacent to zero detuning, i.e., at $\Delta k \approx 1$ FSR. Now, is it possible to engineer $\text{Re}(\gamma)$ so that it becomes positive at a detuning of value other than 1 FSR? Let us consider the case in Fig 4.5(c). Here, the second maximum occurs at $\Delta k \approx 39$ FSRs. Although $\text{Re}[\gamma_{\text{NL}}(\Delta k \approx 39 \text{ FSRs})]$ is higher than $\text{Re}[\gamma_{\text{NL}}(\Delta k \approx 1 \text{ FSR})]$, the former fails to raise $\text{Re}(\gamma)$ to zero before the latter does so. However, by increasing the curvature of $\text{Re}(\gamma_L)$ near zero detuning, we can make it “harder” for $\text{Re}[\gamma(\Delta k \approx 1 \text{ FSR})]$ to reach zero. Also, by decreasing the difference between the heights of the two maxima, we can make it “easier” for the second maximum to reach zero. Thus, if we keep reducing the height difference between the two maxima and/or keep increasing the curvature, at some point the instability will occur at the second maximum. The desired changes to the linear part $\text{Re}(\gamma_L)$ can be brought by varying the length and/or the refractive index of the coating.

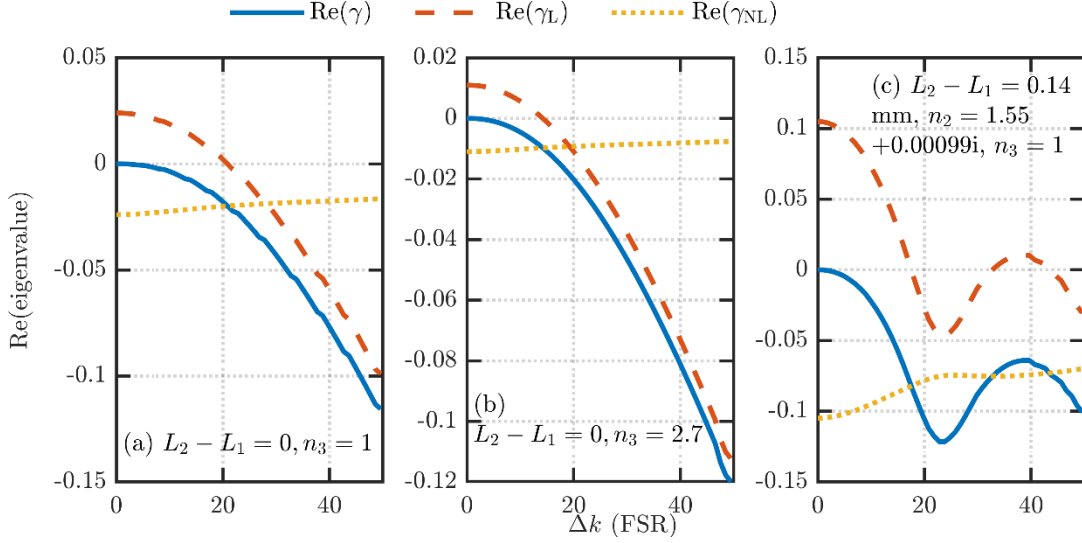


Figure 4.5: Real part of the eigenvalue γ and its breakdown into the linear and nonlinear parts for the same three facet settings considered in Fig. 4.4(a). Pumping level is set to respective p_i .

In Fig. 4.6, we plot W_{th}' and $\text{Re}(\gamma)$ for coating lengths of 0.14, 0.17, 0.3, and 0.45 mm, which depicts the gradual change of the occurrence of instability at 1 FSR to multiple FSRs. The refractive indices of the coating and of the surrounding environment are the same as that in Fig. 4.5(c). Figure 4.6(a) shows that, as the coating length increases, the curvature of W_{th}' around the global minimum increases as well as the difference between the heights of the global minimum and the local minimum adjacent to the global minimum decreases. As a result, the linear part $\text{Re}(\gamma_L)$ undergoes a curvature increase around zero detuning and also experiences a decrease in the difference between the heights of the first two maxima. Therefore, as shown in Fig. 4.6(b), the second maximum of $\text{Re}(\gamma)$ reaches zero before $\text{Re}[\gamma(\Delta k \approx 1 \text{ FSR})]$ for $L_2 - L_1 = 0.3$ and 0.45 mm, resulting in the appearance of harmonic states. In particular, instability occurs at $\Delta k \approx 21$ FSRs for $L_2 - L_1 = 0.3$ mm and at $\Delta k \approx 14$ FSRs for $L_2 - L_1 = 0.45$ mm. We note that these values of the wavevector detuning are close to respective $\pi/[\text{Re}(n_2)(L_2 - L_1)]$, which can be considered as the “FSR” corresponding to the coating section only.

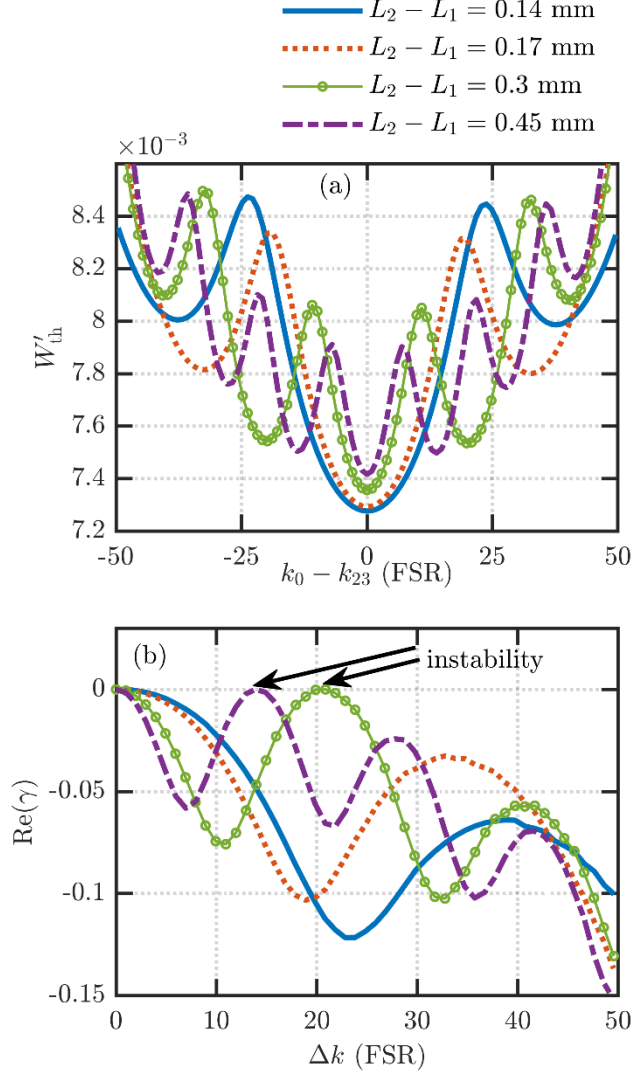


Figure 4.6: (a) Scaled threshold function and (b) real part of γ at the onset of instability for four different coating lengths. The refractive index of the coating is $n_2 = 1.55 + 0.00099i$, and the surrounding environment is assumed to be free space. For coating lengths of 0.14 and 0.17 mm, instability occurs at a wavevector detuning of ~ 1 FSR, whereas for 0.3 and 0.45 mm, instability occurs at ~ 21 and ~ 14 FSRs, respectively.

We now discuss the three-mode regime where the primary mode and the two side modes lase at a steady state. For $p > p_i$, the CF-state coefficients corresponding to the side modes are nonzero, and the primary-mode equation no longer remains independent of the side-mode equations. Therefore, the full equation (4.27), with $G_l(x)$ given by Eq. (4.33), has to be solved iteratively to find $b_{r(l=0,+,-)}$ and k_l . Since the CF wavevectors κ_{rl} depend on k_l , Eq. (4.24) needs

to be solved simultaneously as well. The values obtained from the linear stability analysis can be used as initial values for the iteration. One can verify that Eq. (4.27) is invariant under the transformation $\{b_{r0}\} \rightarrow e^{i\theta_0} \{b_{r0}\}$, $\{b_{r+}\} \rightarrow e^{i\theta_+} \{b_{r+}\}$, and $\{b_{r-}\} \rightarrow e^{i(2\theta_0-\theta_+)} \{b_{r-}\}$, where θ_0 and θ_+ are arbitrary phase angles. Since two free parameters are involved, one needs to vary either k_0 and k_+ or k_0 and k_- in order to implement the GFR; the wavevector of the third mode can be found by noting that the side modes are equally detuned from the primary mode. Figure 4.7 shows the mode intensities (i.e., $20 \log_{10} |F_l/F_0|$) for the same four facet settings that have been considered in Fig. 4.6. The pumping levels used are higher than but close to respective p_i . The side modes lase at wavevectors very close to those predicted by the linear stability analysis. In particular, for coating lengths of 0.14 and 0.17 mm, the spacing between the modes is approximately 1 FSR, whereas for 0.3 and 0.45 mm, the modes are separated by multiple FSRs. In all the cases, side modes behave like an FM wave.

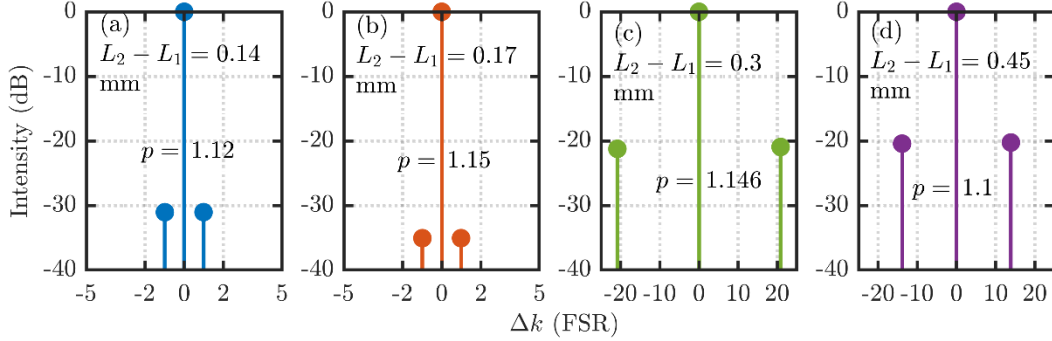


Figure 4.7: Intensities of the primary and side modes for the same four facet settings considered in Fig. 4.6. The pumping levels at which the mode intensities are found are also shown in this figure. The relative phase Θ is approximately -180° in each of the cases.

For harmonic states to appear, W_{th}' does not need to be approximately symmetric like the ones in Fig. 4.6(a). In Fig. 4.8, we show W_{th}' and the corresponding solution of the mode equations for the two facet settings: $L_2 - L_1 = 0.345$ mm with $n_2 = 1.45 + 0.00099i$ and $L_2 - L_1 = 0.4$ mm with $n_2 = 1.71 + 0.00099i$. In both cases, n_3 is taken to be 1. In Fig. 4.8(a), W_{th}' is asymmetric with respect to the global minimum in the sense that the height of the left minimum is greater than

that of the right minimum, whereas W_{th}' in Fig. 4.8(c) is asymmetric with the left minimum being lower than the right minimum. In both cases, harmonic states appear, as shown in Figs. 4.8(b) and 4.8(d). However, the asymmetry in W_{th}' causes the intensities of the side modes to be unequal to some degrees. Since the active region is the same for all our simulations, Figs. 4.7(c), 4.7(d), and 4.8(b) indicate that the spacing between the modes in a harmonic state can be varied by the facet engineering (the mode separations are 21, 14, and 19 FSRs, respectively).

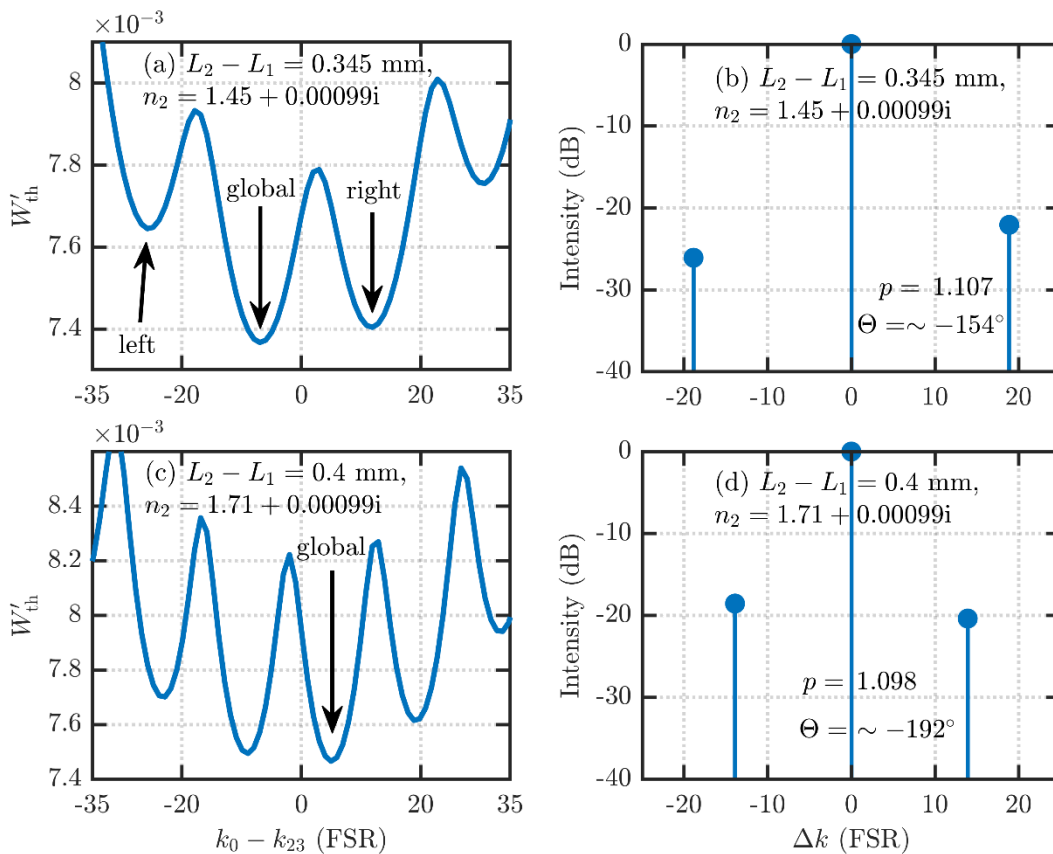


Figure 4.8: (a), (c) Scaled threshold function for two different facet settings, and (b), (d) the corresponding mode intensities. The pumping levels used for the simulation and the corresponding relative phases are also shown in the figure.

4.5 Summary

By taking cavity openness into account, we have presented a theory that describes the

behavior of a primary mode and two side modes in a QCL. We have used CF states to express spatial variations of the modes in an open cavity and thus derived steady-state mode equations that give all relevant information about the three modes. Using our theory, we have shown that, harmonic states with different mode spacing can be excited by varying the length of a facet coating and its refractive index. Namely, facets can be designed so that mirror loss modulates with frequency, which, then, introduces multiple minima in the scaled threshold function of a QCL. If the curvature of the threshold function around the global minimum as well as the difference between the heights of the minima are properly set, harmonic states will appear.

Chapter 5: Conclusion, contribution, and future works

5.1 Conclusion

This thesis has been devoted to understanding of the harmonic state regime of quantum cascade lasers (QCLs). Although operation in this regime is a general phenomenon for QCLs, it was not until 2016 that the regime was conclusively discovered. The reason behind its late discovery is that the harmonic states are very sensitive to external disturbances and hence easily change into the familiar dense states. The facts that this phenomenon is a recent discovery and it has important applications in many areas, such as in picosecond pulse generation and broadband spectroscopy, have provided motivation to perform research in this direction.

For theoretical investigation in this thesis, the coupled density matrix (DM) and Maxwell's equations have been used. Although two-level DM equations were used in most of the previous works, here, instead, three-level DM equations have been employed, which is a more realistic reflection of complex carrier transport through QCLs.

In chapter 3, by employing the closed-cavity approximation (unity facet reflectivity), a closed-form expression for the instability gain of the side modes has been derived. This expression can explain the appearance of harmonic states in QCLs. With the help of this analytical expression, the effects of group velocity dispersion (GVD) on the harmonic states have been studied. In particular, it has been found that, up to a particular value of GVD, side modes behave like a frequency-modulated wave. At higher dispersion, however, they behave neither like a frequency-modulated nor like an amplitude-modulated wave.

In chapter 3, although the diffusion of the zero-frequency population terms has been taken into account, the diffusion of the population-pulsation (PP) terms has been ignored, as done in Ref. [13] as well. However, in a later work [41], it has been shown that if one takes into consideration the diffusion of the PP terms, the analysis (instability gain) fails to explain the origin of the harmonic states.

In chapter 4, multimode behavior of QCLs has been studied using a more general model

than that used in chapter 3. In particular, the diffusion of the PP terms has been included. In addition, and most importantly, openness of the QCL cavity has been accounted for, which was not considered in previous works that used the modal expansion method to study QCLs. In line with Ref. [41], it has been found that when the mentioned diffusion terms are included, the instability gain predicts the appearance of the dense state (single-free-spectral-range-spaced state), not the harmonic states; see Fig. 4.4. However, in experiments, the harmonic states clearly appear. Therefore, the modal analysis is not successful in explaining the origin of the self-starting harmonic states, and this issue remains unresolved to date.

Although the theory/model in chapter 4 does not explicitly explain the origin of the self-starting harmonic states, it does, however, have the capability to suggest a way to excite them. The theory has this capability because of the consideration of cavity openness. Using this theory, it has been demonstrated that the coating of a facet can be exploited to excite harmonic states with different mode spacing. Such a control over the generation of harmonic states could make QCLs invaluable for the previously mentioned applications.

5.2 Contributions

The contribution of this thesis can be summarized below:

- a. A closed-form expression for the instability gain of the side modes has been derived from a coupled three-level DM and Maxwell's equations. The closed-cavity approximation has been employed here. With the help of this analytical expression, the effects of GVD on the harmonic states has been investigated.
- b. A theory to describe multimode behavior of QCLs has been formulated, again from the DM-Maxwell equations, but considering openness of the cavity. Using the theory, it has been demonstrated that one can excite harmonic states with different mode spacing by exploiting the properties of the coating of a facet.

The following publications are the result of this thesis:

1. M. Roy and M. Z. Kabir, "Harmonic instability in a quantum cascade laser with Fabry-Perot cavity," *J. Appl. Phys.* **128**, 043105 (2020).

2. M. Roy and M. Z. Kabir, “Exciting harmonic states in a quantum cascade laser via facet engineering,” *Phys. Rev. A*, under first revision (2021).

5.3 Future works

As mentioned, the modal expansion method has not been able to satisfactorily explain the origin of the self-starting harmonic states in Fabry-Perot QCLs to date. There exists another method for studying multimode behavior of QCLs, namely the space and time domain simulation of Maxwell-Bloch equations. This method, either, has not been able to adequately explain the phenomenon; an external optical seeding is required for this method to reproduce the harmonic states [41], whereas they appear in experiments without any external seeding (hence the name self-starting). Therefore, more theoretical work is needed to identify the origin of the self-starting harmonic states in Fabry-Perot QCLs.

Although the theory in chapter 4 considers cavity openness, it can be improved further as described below. Only three modes, i.e., a primary mode and two side modes, have been included in the theory. Although able to show the way to excite harmonic states, the model does not convey information about the bandwidth of the harmonic states with increasing pumping. For this, more side modes need to be included. Moreover, the Kerr effect, i.e., the change in the refractive index of the material with the intensity of an electromagnetic wave, has not been considered. The inclusion of these factors will make the theory more complete, realistic, and powerful.

Appendix A: Three-level system versus two-level system

In this appendix, we show that the three-level density matrix (DM) equations can be converted to two-level DM equations, and hence, the expressions derived in Sec. 3.3 can also be converted into the corresponding expressions for a system having two energy levels. We also show that the reduced expressions agree with those in Ref. [13].

By subtracting Eq. (3.5) from Eq. (3.6), we find that the population inversion in a three-level system varies according to

$$\dot{\rho}_{22} - \dot{\rho}_{33} = C_2 - \alpha_{13} + (-C_1 - C_4)\rho_{22} - (C_2 - C_5)\rho_{33} + i2aE_z(\rho_{23} - \rho_{23}^*) + D \frac{\partial^2 (\rho_{22} - \rho_{33})}{\partial x^2}. \quad (\text{A1})$$

However, for a two-level system, the population-inversion equation reads

$$\dot{\rho}_{22} - \dot{\rho}_{33} = \frac{w_{\text{eq}} - (\rho_{22} - \rho_{33})}{T_1} + i2aE_z(\rho_{23} - \rho_{23}^*) + D \frac{\partial^2 (\rho_{22} - \rho_{33})}{\partial x^2}, \quad (\text{A2})$$

where T_1 denotes the gain recovery time and w_{eq} is the equilibrium population inversion that would occur in the absence of lasing (the interpretation of w_{eq} is the same as that of W_{eq} ; the difference is that w_{eq} in the two-level system acts as an independent variable, whereas W_{eq} in the three-level system is determined by the energy gap ϵ_{12}). By comparing Eqs. (A1) and (A2), we get

$$C_2 - \alpha_{13} = \frac{w_{\text{eq}}}{T_1} \quad \text{and} \quad C_1 + C_4 = -C_2 + C_5 = \frac{1}{T_1}. \quad (\text{A3})$$

Due to the increased complexity in carrier transport in the three-level model, the parameters C_1 , C_2 , C_4 , C_5 , and α_{13} , all having the unit s^{-1} , arise. Equation (A3) simply describes how these five rates reduce to just two rates, i.e., to the pumping rate w_{eq}/T_1 and the gain recovery rate $1/T_1$, while going from a three-level to a two-level system. Now, if we use Eq. (A3) in Eqs. (3.17) and (3.29) and then plug the latter equation into the former one, W will be reduced to

$$W = W_{\text{th}} \left(1 + \frac{(1+4k_0^2DT_1)^{-1}}{2} \frac{p-1}{1+\frac{(1+4k_0^2DT_1)^{-1}}{2}} - (1+4k_0^2DT_1)^{-1} \frac{p-1}{1+\frac{(1+4k_0^2DT_1)^{-1}}{2}} \cos(2k_0x) \right). \quad (\text{A4})$$

Equation (A4) matches with Eq. (9) in Ref. [13].

Now, we convert the expression of our intensity gain, i.e., $\text{Re}(g_m)+1$ [see Eq. (3.36)], into the corresponding expression for a two-level system by using Eq. (A3) as well as by making the following assumptions: $\omega_0 = \omega_{23}$; $n(\omega_0) = n(\omega_+) = n(\omega_-)$, i.e., group velocity dispersion is zero; $\omega_{\pm} = \Omega_{\pm}$, i.e., the hot- and cold-cavity modes are identical; and $\omega_+/\omega_0 \approx \omega_-/\omega_0 \approx 1$. Thus, we get

$$\begin{aligned} \text{Re}(g_{1,2})+1 &= \left(1 + \frac{(1+4k_0^2DT_1)^{-1}}{2} \frac{p-1}{1+\frac{(1+4k_0^2DT_1)^{-1}}{2}} \right) \frac{1}{1+\delta\omega^2\tau_{\parallel,23}^2} \\ &+ \text{Re} \left(- \frac{1-i\delta\omega\tau_{\parallel,23}/2}{(1-i\delta\omega\tau_{\parallel,23})^2(1-i\delta\omega T_1)} \right) \frac{p-1}{1+\frac{(1+4k_0^2DT_1)^{-1}}{2}} \times \begin{cases} 1/2 \\ 3/2 \end{cases}, \end{aligned} \quad (\text{A5})$$

which is the same as Eq. (19) in Ref. [13]. The agreement of Eqs. (A4) and (A5) with the corresponding equations in Ref. [13] proves that the derivation presented in Sec. 3.3 is correct.

References

- [1] A. E. Siegman, *Lasers* (University Science Books, 1986).
- [2] D. J. Griffiths, *Introduction to Quantum Mechanics* (Prentice Hall, 1995).
- [3] P. Tzenov, “Modeling and simulations of quantum cascade lasers for frequency comb generation,” Ph.D. dissertation (Technical University of Munich, 2019).
- [4] B. Williams, “Terahertz quantum-cascade lasers,” *Nat. Photonics* **1**, 517–525 (2007).
- [5] R. F. Kazarinov and R. A. Suris, “Possibility of the amplification of electromagnetic waves in a semiconductor with a superlattice,” *Soviet Physics-Semiconductors* **5**, 707–709 (1971).
- [6] J. Faist, F. Capasso, D. L. Sivco, C. Sirtori, A. L. Hutchinson, and A. Y. Cho, “Quantum cascade laser,” *Science* **264**, 553–556 (1994).
- [7] M. Beck, D. Hofstetter, T. Aellen, J. Faist, U. Oesterle, M. Illegems, E. Gini, and H. Melchior, “Continuous wave operation of a mid-infrared semiconductor laser at room temperature,” *Science* **295**, 301–305 (2002).
- [8] R. Kohler, A. Tredicucci, F. Beltram, H. Beere, E. Linfield, A. Davies, D. Ritchie, R. Iotti, and F. Rossi, “Terahertz semiconductor-heterostructure laser,” *Nature* **417**, 156–159 (2002).
- [9] A. Khalatpour, A. K. Paulsen, C. Deimert, Z. R. Wasilewski, and Q. Hu, “High-power portable terahertz laser systems,” *Nat. Photonics* **15**, 16–20 (2021).
- [10] A. Bismuto, R. Terazzi, M. Beck, and J. Faist, “Electrically tunable, high performance quantum cascade laser,” *Appl. Phys. Lett.* **96**, 141105 (2010).
- [11] F. Xie, C. G. Caneau, H. P. LeBlanc, M. T. Ho, J. Wang, S. Chaparala, L. C. Hughes, and C.-e. Zah, “High power and high temperature continuous-wave operation of distributed Bragg reflector quantum cascade lasers,” *Appl. Phys. Lett.* **104**, 071109 (2014).
- [12] D. Kazakov, M. Piccardo, Y. Wang, P. Chevalier, T. S. Mansuripur, F. Xie, C.-e. Zah, K. Lascola, A. Belyanin, and F. Capasso, “Self-starting harmonic frequency comb generation in a quantum cascade laser,” *Nat. Photonics* **11**, 789–792 (2017).
- [13] T. S. Mansuripur, C. Vernet, P. Chevalier, G. Aoust, B. Schwarz, F. Xie, C. Caneau, K. Lascola, C. Zah, D. P. Caffey, T. Day, L. J. Missaggia, M. K. Connors, C. A. Wang, A. Belyanin, and F. Capasso, “Single-mode instability in standing-wave lasers: The quantum cascade laser as a self-pumped parametric oscillator,” *Phys. Rev. A* **94**, 063807 (2016).
- [14] M. Piccardo, P. Chevalier, T. S. Mansuripur, D. Kazakov, Y. Wang, N. A. Rubin, L. Meadowcroft, A. Belyanin, and F. Capasso, “The harmonic state of quantum cascade lasers: origin,

- control, and prospective applications [Invited],” *Opt. Express* **26**, 9464–9483 (2018).
- [15] A. Hugi, G. Villares, S. Blaser, H. Liu, and J. Faist, “Mid-infrared frequency comb based on a quantum cascade laser,” *Nature* **492**, 229–233 (2012).
- [16] D. Burghoff, T.-Y. Kao, N. Han, C.W. I. Chan, X. Cai, Y. Yang, D. J. Hayton, J.-R. Gao, J. L. Reno, and Q. Hu, “Terahertz laser frequency combs,” *Nat. Photonics* **8**, 462–467 (2014).
- [17] M. Piccardo, B. Schwarz, D. Kazakov, M. Beiser, N. Opacak, Y. Wang, S. Jha, J. Hillbrand, M. Tamagnone, W. T. Chen, A. Y. Zhu, L. L. Columbo, A. Belyanin, and F. Capasso, “Frequency combs induced by phase turbulence,” *Nature* **582**, 360–364 (2020).
- [18] J. H. Davies, *The Physics of Low-Dimensional Semiconductors* (Cambridge University Press, 1998).
- [19] J. Faist, F. Capasso, C. Sirtori, D. L. Sivco, J. N. Baillargeon, A. L. Hutchinson, S.-N. G. Chu, and A. Y. Cho, “High power mid-infrared ($\lambda \sim 5 \mu\text{m}$) quantum cascade lasers operating above room temperature,” *Appl. Phys. Lett.* **68**, 3680–3682 (1996).
- [20] J. Faist, *Quantum Cascade Lasers* (Oxford University Press, 2013).
- [21] R. W. Boyd, *Nonlinear Optics*, 3rd ed. (Academic, 2008).
- [22] M. A. Talukder, “Modeling of gain recovery of quantum cascade lasers,” *J. Appl. Phys.* **109**, 033104 (2011).
- [23] M. Roy and M. Z. Kabir, “Harmonic instability in a quantum cascade laser with Fabry-Perot cavity,” *J. Appl. Phys.* **128**, 043105 (2020).
- [24] H. Risken and K. Nummedal, “Self-Pulsing in Lasers,” *J. Appl. Phys.* **39**, 4662–4672 (1968).
- [25] R. Graham and H. Haken, “Quantum theory of light propagation in a fluctuating laser-active medium,” *Z. Phys. A: Hadrons Nucl.* **213**, 420–450 (1968).
- [26] C. Y. Wang, L. Diehl, A. Gordon, C. Jirauschek, F. X. Kartner, A. Belyanin, D. Bour, S. Corzine, G. Hofler, M. Troccoli, J. Faist, and F. Capasso, “Coherent instabilities in a semiconductor laser with fast gain recovery,” *Phys. Rev. A* **75**, 031802 (2007).
- [27] A. Gordon, C. Y. Wang, L. Diehl, F. X. Kartner, A. Belyanin, D. Bour, S. Corzine, G. Hofler, H. C. Liu, H. Schneider, T. Maier, M. Troccoli, J. Faist, and F. Capasso, “Multimode regimes in quantum cascade lasers: from coherent instabilities to spatial hole burning,” *Phys. Rev. A* **77**, 053804 (2008).
- [28] N. Vukovic, J. Radovanovic, V. Milanovic, and D. L. Boiko, “Analytical expression for Risken-Nummedal Graham-Haken instability threshold in quantum cascade lasers,” *Opt. Express* **24**, 26911–26929 (2016).

- [29] N. N. Vukovic, J. Radovanovic, V. Milanovic, and D. L. Boiko, “Low-Threshold RNGH Instabilities in Quantum Cascade Lasers,” *IEEE J. Sel. Top. Quantum Electron.* **23**, 1200616 (2017).
- [30] H. Li, P. Laffaille, D. Gacemi, M. Apfel, C. Sirtori, J. Leonardon, G. Santarelli, M. Rosch, G. Scalari, M. Beck, J. Faist, W. Hansel, R. Holzwarth, and S. Barbieri, “Dynamics of ultra-broadband terahertz quantum cascade lasers for comb operation,” *Opt. Express* **23**, 33270 (2015).
- [31] G. Villares and J. Faist, “Quantum cascade laser combs: effects of modulation and dispersion,” *Opt. Express* **23**, 1651–1669 (2015).
- [32] S. T. Hendow and M. Sargent III, “Theory of single-mode laser instabilities,” *J. Opt. Soc. Am. B* **2**, 84–101 (1985).
- [33] R. Terazzi, T. Gresch, A. Wittmann, and J. Faist, “Sequential resonant tunneling in quantum cascade lasers,” *Phys. Rev. B* **78**, 155328 (2008).
- [34] R. Terazzi, T. Gresch, A. Wittmann, and J. Faist, “Erratum: Sequential resonant tunneling in quantum cascade lasers [*Phys. Rev. B* **78**, 155328 (2008)],” *Phys. Rev. B* **83**, 039902 (2011).
- [35] M. Sargent III, M. O. Scully, and W. E. Lamb Jr., *Laser Physics* (Addison-Wesley, 1974).
- [36] Y. K. Chembo and N. Yu, “Modal expansion approach to optical-frequency-comb generation with monolithic whispering-gallery-mode resonators,” *Phys. Rev. A* **82**, 033801 (2010).
- [37] N. Opacak and B. Schwarz, “Theory of Frequency-Modulated Combs in Lasers with Spatial Hole Burning, Dispersion, and Kerr Nonlinearity,” *Phys. Rev. Lett.* **123**, 243902 (2019).
- [38] Y. Wang and A. Belyanin, “Active mode-locking of mid-infrared quantum cascade lasers with short gain recovery time,” *Opt. Express* **23**, 4173–4185 (2015).
- [39] C. Jirauschek and T. Kubis, “Modeling techniques for quantum cascade lasers,” *Appl. Phys. Rev.* **1**, 011307 (2014).
- [40] A. Wittmann, Y. Bonetti, J. Faist, E. Gini, and M. Giovannini, “Intersubband linewidths in quantum cascade laser designs,” *Appl. Phys. Lett.* **93**, 141103 (2008).
- [41] Y. Wang and A. Belyanin, “Harmonic frequency combs in quantum cascade lasers: Time-domain and frequency-domain theory,” *Phys. Rev. A* **102**, 013519 (2020).
- [42] M. Piccardo, P. Chevalier, S. Anand, Y. Wang, D. Kazakov, E. A. Mejia, F. Xie, K. Lascola, A. Belyanin, and F. Capasso, “Widely tunable harmonic frequency comb in a quantum cascade laser,” *Appl. Phys. Lett.* **113**, 031104 (2018).
- [43] F. Wang, V. Pistore, M. Riesch, H. Nong, P.-B. Vigneron, R. Colombelli, O. Parillaud, J. Mangeney, J. Tignon, C. Jirauschek, and S. S. Dhillon, “Ultrafast response of harmonic

modelocked THz lasers,” *Light: Sci. Appl.* **9**, 51 (2020).

[44] A. Forrer, Y. Wang, M. Beck, A. Belyanin, J. Faist, and G. Scalari, “Self-starting harmonic comb emission in THz quantum cascade lasers,” *Appl. Phys. Lett.* **118**, 131112 (2021).

[45] P. Tzenov, D. Burghoff, Q. Hu, and C. Jirauschek, “Time domain modeling of terahertz quantum cascade lasers for frequency comb generation,” *Opt. Express* **24**, 23232–23247 (2016).

[46] D. Burghoff, “Unraveling the origin of frequency modulated combs using active cavity mean-field theory,” *Optica* **7**, 1781–1787 (2020).

[47] J. B. Khurgin, Y. Dikmelik, A. Hugi, and J. Faist, “Coherent frequency combs produced by self frequency modulation in quantum cascade lasers,” *Appl. Phys. Lett.* **104**, 081118 (2014).

[48] H. E. Tureci, A. D. Stone, and B. Collier, “Self-consistent multimode lasing theory for complex or random lasing media,” *Phys. Rev. A* **74**, 043822 (2006).

[49] H. E. Tureci, A. D. Stone, and L. Ge, “Theory of the spatial structure of nonlinear lasing modes,” *Phys. Rev. A* **76**, 013813 (2007).

[50] H. E. Tureci, L. Ge, S. Rotter, and A. D. Stone, “Strong interactions in multimode random lasers,” *Science* **320**, 643–646 (2008).

[51] L. Ge, R. J. Tandy, A. D. Stone, and H. E. Tureci, “Quantitative verification of ab initio self-consistent laser theory,” *Opt. Express* **16**, 16895–16902 (2008).

[52] L. Ge, Y. D. Chong, and A. D. Stone, “Steady-state *ab initio* laser theory: generalizations and analytic results,” *Phys. Rev. A* **82**, 063824 (2010).

[53] O. Zaitsev and L. Deych, “Recent developments in the theory of multimode random lasers,” *J. Opt.* **12**, 024001 (2010).

[54] A. Cerjan, Y. D. Chong, L. Ge, and A. D. Stone, “Steady-state *ab initio* laser theory for n-level lasers,” *Opt. Express* **20**, 474–488 (2012).

[55] A. Cerjan and A. D. Stone, “Steady-state *ab initio* theory of lasers with injected signals,” *Phys. Rev. A* **90**, 013840 (2014).

[56] A. Cerjan, Y. D. Chong, and A. D. Stone, “Steady-state *ab initio* laser theory for complex gain media,” *Opt. Express* **23**, 6455–6477 (2015).

[57] O. Zaitsev and L. Deych, “Diagrammatic semiclassical laser theory,” *Phys. Rev. A* **81**, 023822 (2010).

[58] L. Ge, “Steady-state ab initio laser theory and its applications in random and complex media,” Ph.D. dissertation (Yale University, 2010).